The effect of flame curvature and flame base movement on the frequency response of a conical Bunsen flame

Alessandro Giannotta[1,1], Stefania Cherubini[1], Pietro De Palma[1], Matthew P. Juniper[1]

[a]*Department of Mechanics, Mathematics and Management, Politecnico di Bari, via Re David, 200, Bari, 70125, Italy*

[b]*Department of Engineering, University of Cambridge, Trumpington Street, Cambridge, CB2 1PZ, UK*

Abstract

We create a general model for the tracking of a premixed flame sheet. This model is based on a Lagrangian formulation of the interface motion, which is more computationally efficient than the level-set formulation solved on a grid. We apply this model to a conical Bunsen flame in which flame-base oscillations and flame stretch effects are also considered. We demonstrate that the flame-front dynamics, the heat release rate perturbations, and the flame transfer function (FTF) are affected by three features: (i) the velocity field locally perturbing the flame-front, (ii) the flame-base oscillations normal to the steady flame-front propagating along the flame and (iii) the flame-base oscillations tangential to the flame-front reducing and increasing the flame-length. We provide a physical explanation for the saturation of the FTF phase shift with increasing forcing frequency, which is found experimentally. We show why a $n - \tau$ model with fixed τ cannot model this simple flame and that, when building a quantitatively-accurate model of a thermoacoustic system containing this flame, the flame dynamics need to be simulated directly or modelled more accurately than with the $n - \tau$ model. The flame model used in this paper has been designed to be differentiable so that it can be used for rapid data assimilation using Laplace's method. Code is provided so that the user can generate the FTF of a conical premixed flame with any set of parameters and any flame-base trajectory.

Keywords: Thermoacoustics, Premixed flame response, Flame transfer function, Flame-base motion, Lagrangian front tracking

1. Introduction

There is currently no alternative to combustion for powering long distance air transport, due to the required power-to-weight and energy-to-weight ratios. There is a desire, however, to reduce carbon dioxide (CO2) and nitrous oxide (NOx) emissions. This is motivating research into lean premixed combustion of fossil fuels, sustainable aircraft fuels, and hydrogen

fuel. Lean combustion is a promising technology to reduce NOx emissions because the lower temperatures reduce the thermal NOx. Lean combustion systems are, however, more susceptible to dangerous thermoacoustic oscillations, which motivates continual research in this area.

Combustion instability has been studied since the 19th century [?] but remains an active area of research because of its importance and complexity. If the flame in a combustion chamber is perturbed by velocity or pressure fluctuations, the heat release rate fluctuates [?]. If this unsteady heat release rate occurs sufficiently in phase with pressure oscillations, then heat is converted to work over an oscillation cycle. This is known as the thermoacoustic mechanism. This causes the acoustic energy to increase until the damping and acoustic energy losses due to radiation match the thermoacoustic driving. Usually, this results in periodic limit cycles, although quasi-periodic and chaotic oscillations have also been observed. These oscillations can reduce performance, shorten component lifetimes, cause severe damage, and even lead to catastrophic failure [?].

Combustion instability is difficult to model successfully because the efficiency of the thermoacoustic driving mechanism is highly sensitive to small changes in the device [?]. This means that, even if a model of a thermoacoustic system is qualitatively correct, it may not be sufficiently quantitatively correct to be a useful design tool. Usually, aircraft engines are developed after component tests, then sector tests, then full engine tests. It is not uncommon for thermoacoustic instabilities to appear in the final stages of development, even if models from component tests did not predict it [?]. Fortunately, this sensitivity to small changes also allows combustion instability to be removed with relatively small modifications to the engine. The challenge is to calculate these modifications as quickly as possible, which is where a quantitatively-accurate model is desired, ideally combined with adjoint methods for design [?]. This is a technically difficult process, however, which needs to be developed and tested carefully on canonical flows, which is the subject of this paper.

There are several hundred papers in the literature describing several dozen models for the components of a thermoacoustic system [? ? ?]. It is challenging to select the most pertinent model and, even then, there is no guarantee that parameter values that are accurate for one configuration will remain accurate for another configuration. An alternative approach is to obtain a large amount of data from an experimental rig and to use Bayesian inference to select the best model, by combining data from experiments with prior beliefs about the candidate models and the probability distributions of their parameters [?]. This exploits the convenient fact that, in thermoacoustics, the measurable features such as frequency and growth rate (or limit cycle amplitude), are usually exceedingly sensitive to the model parameters, meaning that the influence of model parameters is usually observable in the data. Examples of data-driven approaches in the context of thermoacoustic instabilities can be found in the studies of Noiray et al. [?], Gant et al. [?] and Ghani et al. [? ?]. In these studies, the authors use pressure time series recorded at specific locations in the combustion chamber during a limit cycle and apply system-identification methods (SI) to infer flame model parameters with the Maximum Likelihood Estimate approach. In particular, Ghani et al. [?] model the flame transfer function of a premixed swirl turbulent flame using the

Distributed Time Delay model of Komarek and Polifke [?], which depends on five physical parameters and infer their values by minimising the discrepancy between experimental data and model predictions. The above studies are particularly relevant when optical access to the flame is not possible. If, however, the flame's natural emissions can be recorded by high-speed cameras, it is possible to use this visual data to tune a physics-based reduced-order model of the flame-front dynamics by minimising the discrepancy between its predictions and the flame images. This model is governed by partial differential equations and gives, amongst other things, the heat release rate as a function of acoustic fluctuations. The final result is a quantitatively-accurate model that is interpretable and extrapolatable. This process only works, however, if models are qualitatively correct - i.e. if they can replicate the observed physics with as few parameters as possible. The assimilation process is greatly accelerated if the model is also differentiable. This is because the gradient of the flame position with respect to the model parameters can be used to minimise the discrepancy between model predictions and flame images using a gradient-descent method.

This paper examines a general model for axisymmetric premixed flames that is differentiable and suitable for rapid data assimilation. We apply this model to an acoustically forced conical Bunsen flame in order to identify the impact of the most influential parameters on the flame transfer function and to determine whether or not it could be replaced with a simpler time delay $(n - \tau)$ model. This type of flame has been studied before both numerically and experimentally. The models adopted in these numerical studies can be divided into high-fidelity CFD models [? ?] and reduced-order models, in which the flame thickness is assumed to be much shorter than the hydrodynamic lengthscale [?]. In the latter models, the flame is modelled as an infinitesimally thin surface that can be tracked explicitly (the front-tracking method, such as that used in the current study) or expressed as the level-set of a time-evolving scalar field, G (the front-capturing method). These level-set methods are based on the G-equation [? ?], which can have analytical solutions when linearized. [? ? ? ? ?]. Analytical derivations are found by assuming that one coordinate can be expressed as a function of the other. These formulations are particularly attractive because they lead to analytical equations for flame shapes and FTFs; moreover, a clear identification of the different contributions of each model parameter is possible. However, they need to either assume that the flame remains anchored to the burner rim or neglect the influence of the flame curvature on the flame speed. Experimental studies [? ? ? ?] have shown, however, that the flame base sits a small distance above the rim and follows an approximately elliptical trajectory when forced. Cuquel et al. [?] develop an analytical framework in which the flame base oscillates normally to the flame front. They assume that the flame speed does not depend on flame stretch (i.e. the Markstein length is zero), which allows them to obtain an analytical expression for the flame transfer function (FTF) in which the contributions from the velocity field perturbations and the flame base oscillations are clearly distinguished. With this assumption, the influence of flame stretch on flame speed is ignored [? ?]. For a more detailed model, this influence must be included in order to prevent the formation of cusps and to capture the decay of wrinkles as they propagate down the flame [?]. The influence of geometric curvature (but not hydrodynamic strain) was included by Orchini and Juniper [?], but only for a flame anchored to the burner rim.

In order to take into account the effects of the flame stretch and to allow the flame-base to follow any possible trajectory, we have developed a front-tracking method based on a Lagrangian formulation of the flame-front. In this case the flame-front is expressed in the laboratory frame by a parametrised curve $\tilde{\mathbf{x}}(\eta, \tilde{t})$, where η is a scalar parameter. On the one hand, this formulation makes the computation of the flame dynamics extremely efficient because the number of degrees of freedom is reduced with respect to a grid-based level-set solver. It is also easier to treat open curves, where the end point follows a given trajectory, which is cumbersome with the level-set method [?]. One attempt with an open curve with fixed end points has been made by Smereka [?]. On the other hand, the level-set method has the advantage of naturally incorporating topological changes, which is fundamental when pockets of unburned gases detach from the flame front. In our case, we are interested in small-amplitude perturbations without pinch-off events so the front-tracking method is appropriate. After applying the desired discretisation scheme, the FTF can be calculated with a single fast matrix multiplication operation. This accelerates the evaluation of the flame response at many design parameters.

The objectives of this research are: (i) to assess the combined effects of the flame curvature and flame-base oscillations on the flame transfer function of a conical Bunsen flame; (ii) to identify the impact of the most influential parameters of the current model on the flame transfer function and on the flame-front dynamics; (iii) to determine whether or not the model can be replaced by a simpler time delay $(n - \tau)$ model; (iv) to provide a physical explanation for the saturation of the FTF phase shift with increasing forcing frequency, as is found experimentally; (v) to provide a code for axisymmetric laminar premixed flames that is differentiable and suitable for rapid data assimilation. Due to the Lagrangian formulation of the flame front adopted in this study, the contributions of the velocity field and the flame-base oscillations can be expressed explicitly. We show through this that the flame transfer function can be decomposed into three terms, which model the local velocity field contribution and the flame base oscillations normal and tangential to the steady flame front. Further, we show examples of how the model parameters impact the flame-front dynamics and the flame transfer function. We show that this model can replicate characteristic features of conical flame dynamics observed in experiments.

In section ?? we define the general laminar premixed flame model, adapt it to a Bunsen burner flame, and define the flame-base trajectory model. In section ?? we describe the numerical methods. In section ?? we report the results of the study, showing the effect of the flame base movement on the flame movement and the FTF. Finally, in section ?? we summarise the results and discuss some future developments.

2. The model

In this section, we introduce a model for laminar premixed flames and customise it for an axisymmetric Bunsen burner flame. In the following paragraphs, the superscript $\tilde{}$ denotes dimensional quantities, an overbar $\bar{}$ denotes mean quantities, a hat $\hat{}$ denotes Fourier components with respect to time or a unit vector, $\|\cdot\|$ denotes the Euclidean norm, and $\tilde{\mathbf{x}}$ indicates

the position in the laboratory frame.

2.1. Laminar Premixed Flame Model

The propagation of a premixed flame is studied by assuming that two separated length scales exist: the flame thickness $\tilde{\delta}_f$ and the hydrodynamic length $\tilde{L}$ associated, for example, with the geometry of the burner or with the average size of the flame front wrinkles. With respect to the hydrodynamic length, the flame is an infinitesimally thin surface dividing the products from the reactants [? ? ?]. Such a surface can be defined as a level set of a field function $\tilde{G}(\tilde{\mathbf{x}}, \tilde{t}) = 0$. A point on this surface moving with velocity $d\tilde{\mathbf{x}}/d\tilde{t}$ (with respect to the laboratory frame) remains on this surface if [? ?]

$$\frac{\partial \tilde{G}}{\partial \tilde{t}} + \frac{d\tilde{\mathbf{x}}}{d\tilde{t}} \cdot \tilde{\nabla}\tilde{G} = 0. \tag{1}$$

We define the flame speed $\tilde{S}_f$ as the normal velocity of the unburnt gas relative to the flame sheet [? ?]:

$$\tilde{S}_f = \left(\frac{d\tilde{\mathbf{x}}}{d\tilde{t}} - \tilde{\mathbf{v}}\right) \cdot \hat{\mathbf{n}}, \tag{2}$$

where $\tilde{\mathbf{v}}$ is the velocity field of the unburnt gas and $\hat{\mathbf{n}}$ is the unit normal vector to the flame sheet pointing towards the unburnt gases. An expression for the flame speed, which takes into account the flame stretch $\tilde{\mathbb{K}}$, is obtained in the form [?]:

$$\tilde{S}_f = \tilde{S}_L - \tilde{\mathcal{M}}\tilde{\mathbb{K}}, \tag{3}$$

where $\tilde{S}_L$ is the laminar flame speed in the absence of flame stretch and $\tilde{\mathcal{M}}$ is known as the Markstein length. Flame stretch is a variable that measures the deformation of the flame front subjected to a non-uniform velocity field and can be expressed as [? ?]

$$\tilde{\mathbb{K}} = \tilde{S}_L\tilde{k} + \tilde{\mathbb{K}}_s. \tag{4}$$

where $\tilde{k}$ is twice the mean curvature of the surface and $\tilde{\mathbb{K}}_s$ is the hydrodynamic strain due to nonuniformities in the velocity field:

$$\tilde{k} = -\tilde{\nabla} \cdot \hat{\mathbf{n}}, \qquad\qquad \tilde{\mathbb{K}}_s = -\hat{\mathbf{n}} \cdot \tilde{\mathbf{E}} \cdot \hat{\mathbf{n}}, \tag{5}$$

where $\tilde{\mathbf{E}} = 1/2 \left(\tilde{\nabla}\tilde{\mathbf{v}} + \tilde{\nabla}\tilde{\mathbf{v}}^T\right)$ is the rate of strain tensor. In order to describe the kinematic behaviour of the flame front, one can directly solve equation (??) or recast the equation for $\tilde{G}$ by expressing the normal vector $\hat{\mathbf{n}}$ by

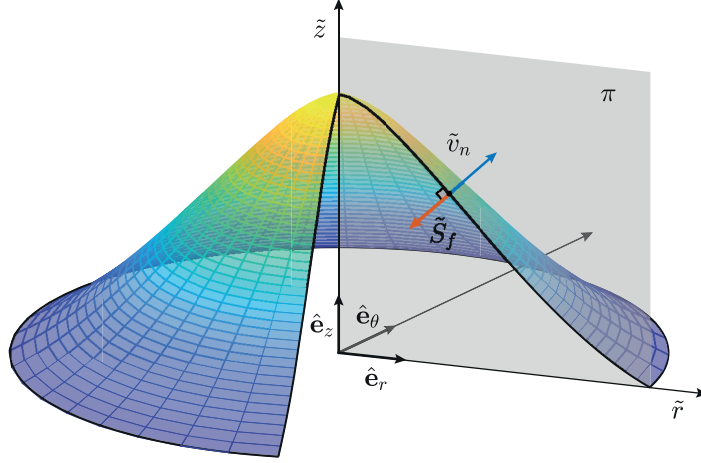$$\hat{\mathbf{n}} = -\frac{\tilde{\nabla}\tilde{G}}{|\tilde{\nabla}\tilde{G}|} \tag{6}$$

Figure 1: Diagram of an axisymmetric flame.

and substituting it into equation (**??**). Using equation (**??**) one obtains the well known G-Equation [**?**]:

$$\frac{\partial \tilde{G}}{\partial \tilde{t}} + \tilde{\mathbf{v}} \cdot \tilde{\nabla} \tilde{G} = \tilde{S}_f |\tilde{\nabla} \tilde{G}|. \tag{7}$$

The two formulations are equivalent. In this study, we adopt the first formulation based on the direct solution of equation (**??**) to provide an efficient computational method, which also allows us to easily describe the movement of the flame-base. In this study, we consider the case of an axisymmetric flame such as that shown in figure **??**. We use a cylindrical reference frame $\Sigma = (0, \tilde{r}, \theta, \tilde{z})$ with corresponding unit vectors $\hat{\mathbf{e}}_r$, $\hat{\mathbf{e}}_\theta$ and $\hat{\mathbf{e}}_z$. We then define a plane section π, perpendicular to $\hat{\mathbf{e}}_\theta$ and passing through the axis of symmetry $\tilde{z}$, and we study the flame behaviour on it taking advantage of the axisymmetry. In order to have a general and yet simple model for premixed flames, which includes the effects of both the flame stretch and flame-base motions, we identify the position of each point on the line representing the flame-front by the vector

$$\tilde{\mathbf{x}}(\eta, \tilde{t}) = \tilde{x}_n(\eta, \tilde{t})\,\hat{\mathbf{n}} + \tilde{x}_t(\eta, \tilde{t})\,\hat{\mathbf{t}} = \tilde{r}(\eta, \tilde{t})\,\hat{\mathbf{e}}_r + \tilde{z}(\eta, \tilde{t})\,\hat{\mathbf{e}}_z, \tag{8}$$

where $\eta \in [0, 1]$ is a parametrisation of the curve representing the flame front and $\hat{\mathbf{t}}$ is the tangential unit vector to the flame front, as shown in figure **??** (a). The proposed model is based on a parametrisation of the flame line because i) such an approach allows us to model complex shapes of the flame, with large deviations from the steady state, by a single-valued function of the parameter η; ii) an arbitrary movement of the flame base can be imposed. The unit vectors $\hat{\mathbf{n}}$ and $\hat{\mathbf{t}}$ can be expressed as

$$\hat{\mathbf{t}} = \frac{1}{\|(\partial_\eta \tilde{r}, \partial_\eta \tilde{z})\|} \left(\partial_\eta \tilde{r}\hat{\mathbf{e}}_r + \partial_\eta \tilde{z}\hat{\mathbf{e}}_z\right), \qquad \hat{\mathbf{n}} = -\hat{\mathbf{t}} \wedge \hat{\mathbf{e}}_\theta = \frac{1}{\|(\partial_\eta \tilde{r}, \partial_\eta \tilde{z})\|} \left(\partial_\eta \tilde{z}\hat{\mathbf{e}}_r - \partial_\eta \tilde{r}\hat{\mathbf{e}}_z\right). \tag{9}$$

6

In the particular case of an axisymmetric surface, the curvature $\tilde{k}$ (defined here as twice the value of the surface mean curvature) is expressed as

$$\tilde{k} = \frac{\partial_\eta \tilde{r} \, \partial_{\eta\eta} \tilde{z} - \partial_{\eta\eta} \tilde{r} \, \partial_\eta \tilde{z}}{\left((\partial_\eta \tilde{r})^2 + (\partial_\eta \tilde{z})^2\right)^{3/2}} + \frac{1}{\tilde{r}} \frac{\partial_\eta \tilde{z}}{\left((\partial_\eta \tilde{r})^2 + (\partial_\eta \tilde{z})^2\right)^{1/2}}. \tag{10}$$

We substitute equation (??) into equation (??), obtaining a system for the radial and longitudinal components of the position vector

$$\begin{cases} \tilde{\partial}_t \tilde{r} &= n_r\left(\tilde{v}_r n_r + \tilde{v}_z n_z + \tilde{S}_f\right), \\ \tilde{\partial}_t \tilde{z} &= n_z\left(\tilde{v}_r n_r + \tilde{v}_z n_z + \tilde{S}_f\right), \end{cases} \tag{11}$$

where the subscripts r and z represent the radial and longitudinal components of any vector such that, for instance, $n_r = \hat{\mathbf{n}} \cdot \hat{\mathbf{e}}_r$ and $n_z = \hat{\mathbf{n}} \cdot \hat{\mathbf{e}}_z$. Finally, after substituting the expressions for the normal vector $\hat{\mathbf{n}}$ (??) and of the curvature $\tilde{k}$ (??) into equation (??), the system of equations (??) is transformed into the following equivalent system of second order nonlinear partial differential equations of the form:

$$\begin{cases} \tilde{\partial}_t \tilde{r} &= \tilde{\mathcal{F}}_1\left(\tilde{t}, \partial_\eta \tilde{r}, \partial_{\eta\eta} \tilde{r}, \partial_\eta \tilde{z}, \partial_{\eta\eta} \tilde{z}, \tilde{\mathbf{p}}\right), \\ \tilde{\partial}_t \tilde{z} &= \tilde{\mathcal{F}}_2\left(\tilde{t}, \partial_\eta \tilde{r}, \partial_{\eta\eta} \tilde{r}, \partial_\eta \tilde{z}, \partial_{\eta\eta} \tilde{z}, \tilde{\mathbf{p}}\right), \end{cases} \tag{12}$$

where $\tilde{\mathbf{p}}$ contains all the physical parameters describing the flame and the velocity field and $\tilde{\mathcal{F}}_1$ and $\tilde{\mathcal{F}}_2$ are known functions. In section ?? we non-dimensionalise the governing equations and we provide their expressions in ??.

2.2. Comparison with state-of-the-art models

This study solves equation (??), rather than equation (??), which was the starting point for previous studies such as [? ?]. Orchini and Juniper [?] used

$$\tilde{G}(\tilde{r}, \tilde{z}, \tilde{t}) = \tilde{z} - \tilde{F}(\tilde{r}) - \varepsilon \tilde{f}(\tilde{r}, \tilde{t}) = 0, \tag{13}$$

where $\tilde{F}(\tilde{r})$ defines the steady flame front and $\tilde{f}(\tilde{r}, \tilde{t})$ defines a perturbation in the longitudinal direction (see figure ?? (b)), and $\varepsilon \ll 1$ defines the perturbation's amplitude. In [?], the effects of the flame curvature on the flame speed are included and the flame-base is anchored to the burner. Experiments [? ? ?] have shown, however, that the flame-base is not anchored to the burner and that its movement must be modelled when calculating the FTF. This is done by Cuquel et al. [?], who assume a zero Markstein length, resulting in a conical flame. They then define a reference system X-Y attached to the steady flame front, as shown in figure ?? (c), and express the scalar field G as:

$$\tilde{G}(\tilde{X}, \tilde{Y}, \tilde{t}) = \tilde{Y} - \tilde{\xi}(\tilde{X}, \tilde{t}) = 0, \tag{14}$$

where $\tilde{Y}$ is the coordinate normal to the steady flame front and $\tilde{\xi}$ its perturbation in the normal direction. Using this model, [?] allows the flame-base to move in the direction

7

normal to the steady flame front. The effects of the flame stretch could not, however, be considered. Both Orchini and Juniper [?] and Cuquel et al. [?] assume that the un-perturbed velocity field is uniform in space, while this study assumes that it is a linear combination of a uniform velocity profile and a parabolic velocity profile.
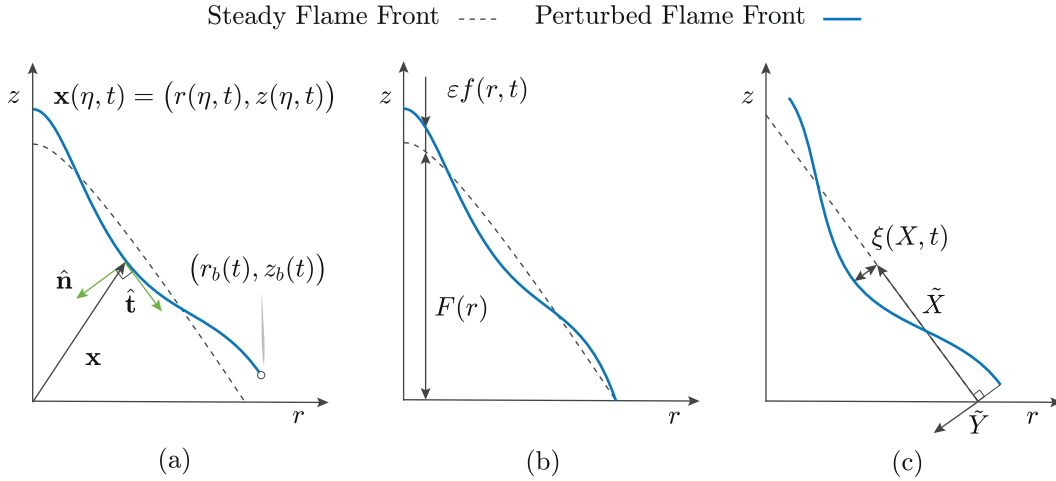
Steady Flame Front ---- Perturbed Flame Front ——

Figure 2: Diagrams of (a) the flame surface in this paper compared with (b) that of Orchini and Juniper[?], and (c) that of Cuquel et al. [?]. The models (b) and (c) both rely on linearisation of the G-Equation expressed by equation (??) for model (b) and equation (??) for model (c). Model (b) includes the effect of flame stretch but the flame-base is anchored to the burner rim and the steady component of the velocity field is uniform. Model (c) does not include the effect of flame stretch, which leads to nonphysical flame tip dynamics, but allows the flame base to move on a straight line perpendicular to the steady flame front. The model in this paper is based on equation (??). The flame front is described by a parameterised curve with the parameter η in the interval $I = [0,1]$ and the flame-base can follow any trajectory. Models (b) and (c) are therefore special cases of model (a).

2.3. Bunsen burner flame

We apply the model described in section ?? to an acoustically forced axisymmetric Bunsen burner flame. The system of equations (??) is completed by the initial condition $\big(\tilde{r}(\eta, 0), \tilde{z}(\eta, 0)\big)$ and the following four boundary conditions:

$$\tilde{r}(\eta = 1, \tilde{t}) = \tilde{r}_b(\tilde{t}), \qquad \tilde{z}(\eta = 1, \tilde{t}) = \tilde{z}_b(\tilde{t}), \qquad \tilde{r}(\eta = 0, \tilde{t}) = 0, \qquad \partial_\eta \tilde{z}(\eta = 0, \tilde{t}) = 0,$$

(15a-d)

where $\tilde{r}_b$ and $\tilde{z}_b$ are the flame-base coordinates, which depend on the chosen trajectory, as discussed in section ??.

Experimental studies on acoustically perturbed conical flames [? ? ?] have shown that harmonic acoustic forcing with angular frequency $\tilde{\omega}$ generates a perturbation of the unburnt gases' incompressible velocity field. Such a perturbation takes the form of a wave originating at the burner rim and travelling along the longitudinal direction with constant phase speed $\tilde{V}_c$ and angular frequency $\tilde{\omega}$. Therefore, we assume that the velocity field $\tilde{\mathbf{v}}$ of the unburnt

8

gases is composed of a steady mean component $\tilde{\mathbf{V}}$ and a small perturbation $\varepsilon\tilde{\mathbf{v}}'$, namely $\tilde{\mathbf{v}} = \tilde{\mathbf{V}} + \varepsilon\tilde{\mathbf{v}}'$, where ε is the amplitude of the acoustic forcing. This assumption implies that the amplitude of the acoustic velocity perturbation at the burner lip equals the amplitude of the unburnt gases velocity field perturbation $\tilde{\mathbf{v}}'$ [? ?]. For simplicity, we assume that the mean flow has no component in the radial direction and that it is a function of the radial coordinate only: $\tilde{\mathbf{V}} = \tilde{V}(\tilde{r})\hat{\mathbf{e}}_z$. We also neglect the feedback effect of the flame-front dynamics on the fresh gas velocity field. This is the main limitation of our model but is acceptable for the purpose of this study. To account for the fact that the nozzle converges just upstream of the flame, the steady velocity field $\tilde{V}(\tilde{r})$ is modelled as a linear combination of a uniform flow and a Poiseuille flow [?] (see figure ??) such that:

$$\tilde{V}(\tilde{r}) = \bar{\tilde{V}}\left(1 + \mu(1 - 2(\tilde{r}/\tilde{R})^2)\right), \tag{16}$$

where μ is a shape parameter in the range $[0, 1]$. When $\mu = 0$, the flow is uniform in the radial direction and when $\mu = 1$, the flow is parabolic. The velocity model does not attempt to resolve the boundary layer at the wall and violates the no slip condition within the burner tube. Outside the burner tube, however, the velocity will relax to a profile that is non-zero everywhere, and since the flame is stabilised at a stand-off distance from the burner, the fresh-gas velocity profile that we prescribe there is not un-physical. Finally, we express the velocity field perturbation $\tilde{\mathbf{v}}'$ as [? ? ? ? ?]

$$\tilde{\mathbf{v}}'(\tilde{r}, \tilde{t}) = \bar{\tilde{V}}\cos\left(\tilde{\omega}\tilde{t} - \tilde{k}_c\tilde{z}\right)\hat{\mathbf{e}}_z - \frac{\bar{\tilde{V}}\tilde{k}_c\tilde{r}}{2}\sin\left(\tilde{\omega}\tilde{t} - \tilde{k}_c\tilde{z}\right)\hat{\mathbf{e}}_r, \tag{17}$$

where $\tilde{k}_c = \tilde{\omega}/\tilde{V}_c$ is the wave number of the harmonic wave. The total velocity field is then

$$\tilde{\mathbf{v}} = -\varepsilon\frac{\bar{\tilde{V}}\tilde{k}_c\tilde{r}}{2}\sin\left(\tilde{\omega}\tilde{t} - \tilde{k}_c\tilde{z}\right)\hat{\mathbf{e}}_r + \bar{\tilde{V}}\left(1 + \mu(1 - 2(\tilde{r}/\tilde{R})^2) + \varepsilon\cos\left(\tilde{\omega}\tilde{t} - \tilde{k}_c\tilde{z}\right)\right)\hat{\mathbf{e}}_z. \tag{18}$$

Using this velocity field, the hydrodynamic strain $\tilde{\mathbb{K}}_s$ is

$$\tilde{\mathbb{K}}_s = \frac{d\tilde{V}}{d\tilde{r}}\frac{\partial_\eta\tilde{r}\,\partial_\eta\tilde{z}}{(\partial_\eta\tilde{r})^2 + (\partial_\eta\tilde{z})^2} + O(\varepsilon) = -\frac{4\mu\tilde{r}\bar{\tilde{V}}}{\tilde{R}^2}\frac{\partial_\eta\tilde{r}\,\partial_\eta\tilde{z}}{(\partial_\eta\tilde{r})^2 + (\partial_\eta\tilde{z})^2} + O(\varepsilon). \tag{19}$$

2.4. Heat release rate

The total heat release rate of the flame $\tilde{q}(\tilde{t})$, in dimensional form, is expressed as:

$$\tilde{q}(\tilde{t}) = \int_{\partial\Omega}\tilde{\rho}_R\tilde{S}_f\tilde{h}_R d\tilde{A}, \tag{20}$$

where $\partial\Omega$ is the total flame area, $\tilde{\rho}_R$ is the reactant's density, $\tilde{h}_R$ is the heat release rate per unit mass of burnt reactants, and $d\tilde{A}$ is an infinitesimal flame area. Assuming an axisymmetric flame, the infinitesimal area $d\tilde{A}$ is evaluated as

$$d\tilde{A} = \tilde{r}d\theta d\tilde{l}, \tag{21}$$

9

where

$$\mathrm{d}\tilde{l} = \|\partial_\eta \tilde{\mathbf{x}}\| = \sqrt{(\partial_\eta \tilde{r})^2 + (\partial_\eta \tilde{z})^2}. \tag{22}$$

Therefore, the instantaneous heat release rate $\tilde{q}$ is

$$\tilde{q}(\tilde{t}) = 2\pi \tilde{\rho}_R \tilde{h}_R \int_0^1 \tilde{S}_f \tilde{r} \sqrt{(\partial_\eta \tilde{r})^2 + (\partial_\eta \tilde{z})^2} \mathrm{d}\eta. \tag{23}$$

2.5. Non-dimensionalisation

The reference speed is the mean value of the velocity field $\bar{\tilde{V}}$; axial distances are scaled by $\tilde{L}_f$, which represents the longitudinal length of the steady flame in the case $\mu = 0$ and $\tilde{\mathcal{M}} = 0$; radial distances are scaled by the burner radius $\tilde{R}$. The ratio of these two reference lengths, $\beta = \tilde{L}_f/\tilde{R}$, is the flame aspect ratio. Time is non-dimensionalised by $\tilde{L}_f/\bar{V}$. In summary, the non-dimensional variables are defined through:

$$\tilde{v}_r = \bar{\tilde{V}} v_r \qquad \tilde{v}_z = \bar{\tilde{V}} v_z \qquad \tilde{z} = \tilde{L}_f z \qquad \tilde{r} = \tilde{R} r \tag{24a}$$

$$\tilde{t} = \frac{\tilde{L}_f}{\bar{\tilde{V}}} t \qquad \beta = \frac{\tilde{L}_f}{\tilde{R}} \qquad \frac{\tilde{S}_L}{\bar{\tilde{V}}} = \frac{1}{\sqrt{1+\beta^2}} \qquad \tilde{\mathcal{M}} = \tilde{L}_f \mathcal{M} \tag{24b}$$

We also introduce the Strouhal number $\mathrm{St} = \tilde{\omega} \tilde{L}_f / \bar{\tilde{V}}$ and the ratio between the velocity
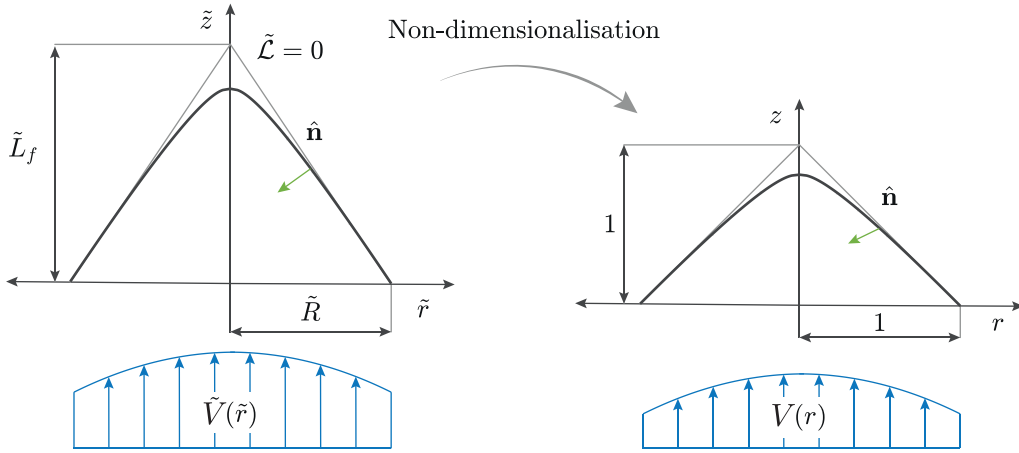

Figure 3: Schematic representation of the flame and the non-dimensionalisation.

perturbation phase speed, $\tilde{V}_c$, and the mean value of the velocity field, $\bar{\tilde{V}}$, $K = \bar{\tilde{V}}/\tilde{V}_c$. The non-dimensional velocity components $v_r(\eta, t)$ and $v_z(\eta, t)$ are then written as $v_r(\eta, t) = \varepsilon v_r'(\eta, t)$ and $v_z(\eta, t) = \bar{v}_z(\eta) + \varepsilon v_z'(\eta, t)$, where $\bar{v}_z(\eta) = 1 + \mu(1 - 2(r(\eta))^2)$ and the acoustic velocity perturbation in phasor notation is written as

$$v_r'(\eta, t) = \mathrm{Re}(\hat{v}_r(\eta) e^{\mathrm{iSt}\, t}), \qquad\qquad v_z'(\eta, t) = \mathrm{Re}(\hat{v}_z(\eta) e^{\mathrm{iSt}\, t}), \tag{25a-b}$$

where

$$\hat{v}_r(\eta) = \mathrm{i}\frac{K\mathrm{St}}{2\beta}r\mathrm{e}^{-\mathrm{i}\mathrm{St}\kappa z}, \qquad\qquad \hat{v}_z(\eta) = \mathrm{e}^{-\mathrm{i}\mathrm{St}\kappa z}. \qquad (26\text{a-b})$$

In the following text we use phasor notation but, for simplicity, drop Re. The stand-off distance is also scaled by the flame length $\tilde{L}_f$:

$$\tilde{\psi}_f = \tilde{L}_f \psi_f. \qquad (27)$$

Due to the different scaling of the radial and longitudinal axes, the normal vector $\hat{\mathbf{n}}$ is no longer perpendicular to the curve in the non-dimensional axes, as shown in figure **??**. When non-dimensional variables are used, $\hat{\mathbf{n}}$ is expressed as

$$\hat{\mathbf{n}} = \frac{1}{\|(\partial_\eta r,\, \beta\partial_\eta z)\|} \left(\partial_\eta \beta z \hat{\mathbf{e}}_r - \partial_\eta r \hat{\mathbf{e}}_z \right). \qquad (28)$$

The heat release rate in equation (**??**) can be expressed as $\tilde{q}(\tilde{t}) = \tilde{q}_{ref}q(t)$, where $\tilde{q}_{ref}$ and $q(t)$ are the reference and non-dimensional heat release rate, respectively:

$$\tilde{q}_{ref} = 2\pi\tilde{\rho}_R\tilde{h}_R\tilde{R}^2\tilde{\bar{V}} \qquad\qquad q(t) = \int_0^1 S_f r\sqrt{(\partial_\eta r)^2 + (\partial_\eta \beta z)^2}\,\mathrm{d}\eta, \qquad (29\text{a-b})$$

where

$$S_f = \tilde{S}_f/\tilde{\bar{V}} = \frac{1}{\sqrt{1+\beta^2}}(1 - \mathcal{M}k) - \mathcal{M}\mathbb{K}_s \qquad (30)$$

is the non-dimensional flame speed. Finally, the non-dimensional form of the system of equations (**??**) governing the movement of the flame is:

$$\begin{cases} \partial_t r &= \mathcal{F}_1\left(t, \partial_\eta r, \partial_{\eta\eta} r, \partial_\eta z, \partial_{\eta\eta} z, \mathbf{p}\right), \\ \partial_t z &= \mathcal{F}_2\left(t, \partial_\eta r, \partial_{\eta\eta} r, \partial_\eta z, \partial_{\eta\eta} z, \mathbf{p}\right). \end{cases} \qquad (31)$$

The expressions for functions $\mathcal{F}_1$ and $\mathcal{F}_2$ are reported in **??**.

2.6. Steady equations

In steady conditions, the non-dimensional hydrodynamic strain $\bar{\mathbb{K}}_s = \tilde{\bar{\mathbb{K}}}_s\tilde{L}_f/\tilde{\bar{V}}$ is expressed as

$$\bar{\mathbb{K}}_s = -4\mu\bar{r}\beta^2\frac{\partial_\eta\bar{r}\partial_\eta\bar{z}}{(\partial_\eta\bar{r})^2 + \beta^2(\partial_\eta\bar{z})^2} \qquad (32)$$

and the non-dimensional curvature $\bar{k} = \tilde{\bar{k}}\tilde{L}_f$ can be written as

$$\bar{k} = \beta^2\left(\frac{\partial_\eta\bar{r}\,\partial_{\eta\eta}\bar{z} - \partial_{\eta\eta}\bar{r}\,\partial_\eta\bar{z}}{\left((\partial_\eta\bar{r})^2 + (\beta\partial_\eta\bar{z})^2\right)^{3/2}} + \frac{1}{\bar{r}}\frac{\partial_\eta\bar{z}}{\left((\partial_\eta\bar{r})^2 + (\beta\partial_\eta\bar{z})^2\right)^{1/2}} \right). \qquad (33)$$

11

Dropping the time derivative terms in equation (**??**) and considering the velocity field given by equation (**??**), one obtains the following equation for the steady-state flame shape $\big(\bar{r}(\eta), \bar{z}(\eta)\big)$:

$$\Big(1 + \mu\big(1 - 2\bar{r}^2\big)\Big)\bar{n}_z + \frac{1}{\sqrt{1 + \beta^2}}(1 - \mathcal{M}\bar{k}) - \mathcal{M}\bar{\mathbb{K}}_s = 0. \tag{34}$$

Therefore, the steady flame sheet is uniquely defined by setting the parameters β, $\mathcal{M}$, μ and the appropriate boundary conditions.

2.7. Flame-base model

Using the flame model presented in section **??**, any time-dependent trajectory of the flame-base can be imposed. Such a trajectory can be directly inferred from experiments, from numerical simulations of the flame-base interaction with the velocity field, or from a low order model of the behaviour of the flame base such as that in [**?**] or the one described in this section. Both Mejia et al. [**?**] and Cuquel et al. [**?**] have tracked the flame-base trajectory experimentally. It can be modelled by an ellipse centred at the base point, whose major axis forms an angle $\theta < \pi/2$ with respect to the radial direction, as shown in figure **??**. We indicate with λ the length of the major axis and with A_R the aspect ratio, so that the
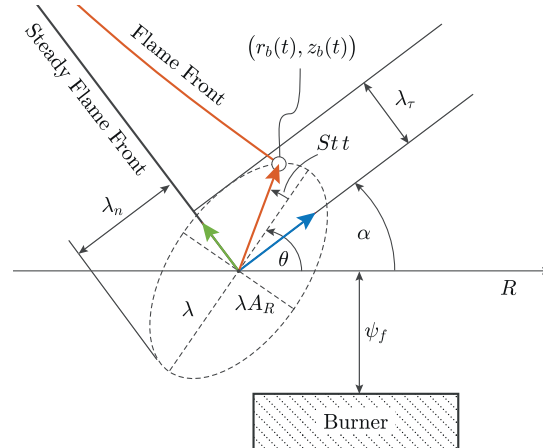

Figure 4: Kinematic diagram of the elliptical flame-base trajectory.

minor axis is equal to the product of λA_R. We assume that the amplitude of the trajectory is proportional to the acoustic forcing amplitude ε and that the flame-base point completes its orbit in the same period of the acoustic forcing (see equations (**??**)). Therefore, the position of the flame base is expressed as $r_b(t) = \bar{r}_b + \varepsilon r_b'(t)$ and $z_b(t) = \bar{z}_b + \varepsilon z_b'(t)$, where $\bar{r}_b$ and $\bar{z}_b$ indicate the non-dimensional radial and longitudinal steady-state coordinates of the flame-base position and

$$r_b'(t) = \lambda\big(\cos(\theta) + \mathrm{i}A_R\sin(\theta)\big)\,\mathrm{e}^{\mathrm{i}(\mathrm{St}\,t + \phi_0)}, \qquad z_b'(t) = \lambda(\sin(\theta) - \mathrm{i}A_R\cos(\theta))\mathrm{e}^{\mathrm{i}(\mathrm{St}\,t + \phi_0)},$$

$$\tag{35a-b}$$

represent their perturbation in phasor notation; the angle ϕ_0 is the initial phase included in the model to allow an additional degree of freedom for the flame-base movement. The angle

α in figure **??** is the angle that the steady flame front forms with the longitudinal axis z at the flame-base. This is useful for decomposing the flame-base motions into the normal and tangential components to the steady-flame line such that

$$r'_b(t) = x_{b,n}(t)\cos(\alpha) - x_{b,t}(t)\sin(\alpha), \qquad z'_b = x_{b,n}(t)\sin(\alpha) + x_{b,t}(t)\cos(\alpha), \qquad \text{(36a-b)}$$

where

$$x_{b,n}(t) = \lambda_n e^{i(\text{St}\,t+\phi_0)}, \qquad\qquad x_{b,t}(t) = \lambda_t e^{i(\text{St}\,t+\phi_0)}, \qquad\qquad \text{(37a-b)}$$

are the normal and tangential flame base movement components, respectively and

$$\lambda_n = \lambda\left(\cos(\theta-\alpha) + iA_R\sin(\theta-\alpha)\right), \qquad \lambda_t = \lambda\left(\sin(\theta-\alpha) - iA_R\cos(\theta-\alpha)\right), \qquad \text{(38a-b)}$$

are complex numbers, whose absolute values correspond to the maximum displacements in the normal and tangential direction, as shown in figure **??**. In section **??**, it is shown that these components have two distinctive effects on the heat release rate.

2.8. Linearisation

If the amplitude of the acoustic forcing is small enough ($\varepsilon \ll 1$), we can find a solution of system (**??**) by reconstructing its first-order approximation assuming that

$$r(\eta, t) = \bar{r}(\eta) + \varepsilon r'(\eta, t) + O(\varepsilon^2), \qquad z(\eta, t) = \bar{z}(\eta) + \varepsilon z'(\eta, t) + O(\varepsilon^2). \qquad \text{(39a-b)}$$

Substituting equations (**??**a) and (**??**b) into $\mathcal{F}_1$ and $\mathcal{F}_2$ of system (**??**), performing a Taylor expansion about $\varepsilon = 0$, and neglecting higher-order terms in ε, we obtain a system of linear equations for the perturbation components r' and z' of the type:

$$\partial_t r' = a_{11}r' + a_{12}\partial_\eta r' + a_{13}\partial_{\eta\eta}r' + a_{14}z' + a_{15}\partial_\eta z' + a_{16}\partial_{\eta\eta}z' + b_1 e^{i\text{St}\,t}, \qquad \text{(40a)}$$

$$\partial_t z' = a_{21}r' + a_{22}\partial_\eta r' + a_{23}\partial_{\eta\eta}r' + a_{24}z' + a_{25}\partial_\eta z' + a_{26}\partial_{\eta\eta}z' + b_2 e^{i\text{St}\,t}, \qquad \text{(40b)}$$

where the coefficients of the linear PDEs $a_{ij} = a_{ij}(\eta)$, $b_i = b_i(\eta, \text{St})$, with $i = 1,2$ and $j = 1,...,6$ are functions of the steady-state flame coordinates $\bar{r}$ and $\bar{z}$, which are found by solving equation (**??**). In particular, the coefficients b_1 and b_2 contain terms from the velocity field and are therefore also functions of the Strouhal number St. The same procedure is applied to the non-dimensional heat release rate $q(t)$: we reconstruct its first-order approximation $q(t) = \bar{q} + \varepsilon q'(t)$; then we substitute equations (**??**a) and (**??**b) into equation (**??**b) obtaining an equation for the heat release rate perturbation of the form

$$q' = \int_0^1 \left(c_1 r' + c_2\partial_\eta r' + c_3\partial_{\eta\eta}r' + c_4 z' + c_5\partial_\eta z' + c_6\partial_{\eta\eta}z'\right) d\eta, \qquad \text{(41)}$$

where the coefficients $c_n = c_n(\eta)$, with $n = 1,...,6$ are functions of the steady-state flame coordinates $\bar{r}$ and $\bar{z}$, which are found by solving equation (**??**). Also the perturbation components r' and z' can be expressed in terms of Fourier components, such that $r'(\eta, t) =$

$\hat{r}(\eta)\mathrm{e}^{\mathrm{iSt}\,t}$ and $z'(\eta,t) = \hat{z}(\eta)\mathrm{e}^{\mathrm{iSt}\,t}$. Substituting these expressions into equations (**??**a) and (**??**b) we obtain the following system:

$$\left(\mathrm{iSt}\mathbf{I} - \begin{pmatrix} a_{11} + a_{12}\partial_\eta + a_{13}\partial_{\eta\eta} & a_{14} + a_{15}\partial_\eta + a_{16}\partial_{\eta\eta} \\ a_{21} + a_{22}\partial_\eta + a_{23}\partial_{\eta\eta} & a_{24} + a_{25}\partial_\eta + a_{26}\partial_{\eta\eta} \end{pmatrix}\right) \begin{pmatrix} \hat{r} \\ \hat{z} \end{pmatrix} = \begin{pmatrix} b_1 \\ b_2 \end{pmatrix} \tag{42}$$

where $\mathbf{I}$ is the identity matrix, which is solved once boundary conditions have been imposed on $\hat{r}$ and $\hat{z}$. The expressions for the coefficients can be found in the code supplied with this paper.

2.9. Flame transfer function

We define the flame transfer function FTF as the ratio between the Fourier components of the heat release rate normalised by the mean heat release rate, $\hat{q}$, and the longitudinal component of the acoustic velocity field measured at the burner rim normalised by the mean flow velocity, $\hat{u}$, at angular frequency St. We assume, for simplicity, that the longitudinal component of the unburnt gas velocity perturbation is equal to the acoustic velocity perturbation at the burner rim $\hat{v}_z(z = -\psi_f) = \hat{u}$ [**?**]. Substituting $z = -\psi_f$ into equation (**??**b), $\hat{u}$ is expressed as

$$\hat{u} = \mathrm{e}^{-\mathrm{iSt}K(-\psi_f)}. \tag{43}$$

Because equation (**??**) is linear, we can employ the superposition principle and express the heat release rate (and therefore the FTF) as the sum of three contributions: the first, $\hat{q}_v$, is caused by the velocity field perturbation; the other two, $\hat{q}_n$ and $\hat{q}_t$, are caused by motions of the flame base in the normal and tangential directions with respect to the steady-state flame at the flame base, respectively. Therefore, the FTF can be expressed as

$$FTF = \frac{\hat{q}}{\hat{u}} = \frac{\hat{q}_v}{\hat{u}} + \frac{\hat{q}_n}{\hat{u}} + \frac{\hat{q}_t}{\hat{u}}. \tag{44}$$

The flame transfer functions corresponding to flame base motions can be expressed as

$$FTF_n = \frac{\hat{q}_n}{\hat{u}} = \frac{\hat{q}_n}{\lambda_n} \frac{\lambda_n}{\hat{v}_n(0)} \frac{\hat{v}_n(0)}{\hat{u}} \tag{45a}$$

$$FTF_t = \frac{\hat{q}_t}{\hat{u}} = \frac{\hat{q}_t}{\lambda_t} \frac{\lambda_t}{\lambda_n} \frac{\lambda_n}{\hat{v}_n(0)} \frac{\hat{v}_n(0)}{\hat{u}} \tag{45b}$$

where the factor λ_t/λ_n takes into account the geometrical properties of the flame-base trajectory. The transfer function $\lambda_n/\hat{v}_n(0)$ links the normal flame-base oscillations to the local velocity field perturbation and can be expressed through the model proposed by Rook et al. [**?**] as in [**?**].

3. Numerical Methods

The governing equations (**??**) are discretized in η by a uniform 1D mesh using $N = 200$ nodes. The first and second derivatives with respect to η, ∂_η and $\partial_{\eta\eta}$, are discretised with
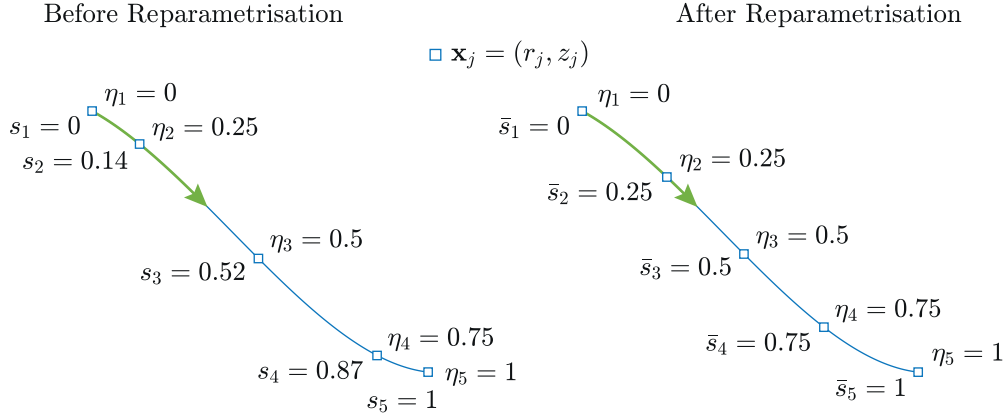
Figure 5: Diagram of the reparametrisation step on a generic curve $\mathbf{x}$ of length $l = 1$, where, for simplicity, it has been assumed that the parameter η is discretised on a uniform grid of five nodes. The square markers represent the points on the η-grid before and after the reparametrisation step.

a second-order accurate central finite difference scheme. The system is marched forward in time by a fifth-order accurate embedded Runge-Kutta scheme. The steady-state equation (**??**) is solved by assuming $\eta_j = r_j$, with the index $j = 1, .., 200$, and then solved numerically for z_j using a Newton-Raphson method.

The accuracy of the time marching solution is improved by imposing that the finite number of points defining the flame front are approximately equidistant from each other. At the beginning of each time step, the curve is re-parametrised. We consider the arc-length $s(\eta)$ (or natural parameter)

$$s(\eta) = \int_0^{\eta} \|\partial_{\bar{\eta}}\mathbf{x}\| \, d\bar{\eta}, \tag{46}$$

of the curve $\mathbf{x}$ identifying the flame front. In discrete form, equation (**??**) is

$$s_j \approx \sum_{n=1}^{j} \|\partial_{\eta}\mathbf{x}\|_n \Delta\eta, \tag{47}$$

where s_j denotes the arc-length corresponding to the j-th node of the η-grid, so that the length of the curve $\mathbf{x}$ can be approximated by s_N, where N is the number of nodes of the η-grid. The values of s_j also define a non-uniform grid with corresponding values for r_j and z_j. Therefore, the idea is to interpolate the values of r_j and z_j onto a uniform grid $\bar{s}_j$ at each time-step, where the $\bar{s}$-grid is obtained by dividing the total length of the curve $\mathbf{x}$ into N equal parts, such that $\bar{s}_{j+1} - \bar{s}_j = s_N/N$. An illustrative diagram is shown in figure **??**. Finally, the integrals in equations (**??**) and (**??**) are solved by employing the trapezoidal rule.

The computational cost of this Lagrangian formulation is significantly lower compared to that of the level-set method, which would require an $N \times N$ 2D Cartesian grid to achieve approximately the same spatial resolution. A reduction of the computational cost can be achieved by employing the local level-set approach [**?**] as in Hemchandra [**?**].

4. Contribution to the FTF from flame-base oscillations

We introduce the parameter $K_f = (1 + \beta^2)/\beta^2$, which is the convection speed of flame shape perturbations when $\mathcal{M} = 0$ (see equation (12) in [?]). When $K = K_f$ the velocity perturbations and the flame disturbances are convected at the same speed. We also introduce the modified Strouhal number $\text{St}_2 = \text{St}(1 + \beta^2)/\beta^2$, which corresponds to ω^* in [?].

4.1. Tangential component $\bar{F}_t$

Let us consider the first term on the r.h.s. of equation (??b). This is the ratio of the heat release rate perturbation due to flame-base tangential movement, $\hat{q}_t$, and the tangential component of the flame-base movement, λ_t:

$$\bar{F}_t = \frac{\hat{q}_t}{\lambda_t}. \tag{48}$$

This movement varies the flame length without changing its shape. According to equations (??a-b) and (??a-b), the flame-base coordinates $r'_b(t)$ and $z'_b(t)$ follow

$$r'_b(t) = -\lambda_t \sin(\alpha) e^{i(\text{St}\, t + \phi_0)}, \qquad z'_b(t) = \lambda_t \cos(\alpha) e^{i(\text{St}\, t + \phi_0)}. \tag{49a-b}$$

In the case of zero Markstein length, $\mathcal{M} = 0$, the heat release rate $\hat{q}_t$ is equal to the flame area ratio $\hat{A}_t/\bar{A}$. Moreover, the flame shape is a cone with area $A(t) = \pi R(t)L(t)$, where $R(t)$ and $L(t)$ are the cone radius and side length, respectively. In this case the flame area is:

$$A(t) = \pi R(t)L(t) = \pi \left(R - \lambda_t e^{i(\text{St}\, t + \phi_0)} \cos(\alpha) \right) \left(R\sqrt{1 + \beta^2} - \lambda_t e^{i(\text{St}\, t + \phi_0)} \right). \tag{50}$$

Hence,

$$\bar{F}_t = \frac{\hat{A}/\bar{A}}{\lambda_t/R} = -\frac{2}{\sqrt{1 + \beta^2}}. \tag{51}$$

Therefore, $\bar{F}_t$ has the same gain at all frequencies, and a constant phase shift equal to $-\pi$. For non-zero values of the Markstein length, one obtains the results reported in figure ?? showing the gain, phase and polar plot of the transfer function $\bar{F}_t$ computed with $\mathcal{M} = 0, 0.001, 0.005, 0.01$. Such results confirm that the flame stretch has a negligible influence on the transfer function $\bar{F}_t$, which can be well approximated by the analytical solution reported in equation (??).

4.2. Normal component $\bar{F}_n$

Let us consider the first term on the r.h.s. of equation (??a), which is the ratio of the heat release perturbation due to flame-base normal oscillations, $\hat{q}_n$, and their amplitude λ_n;

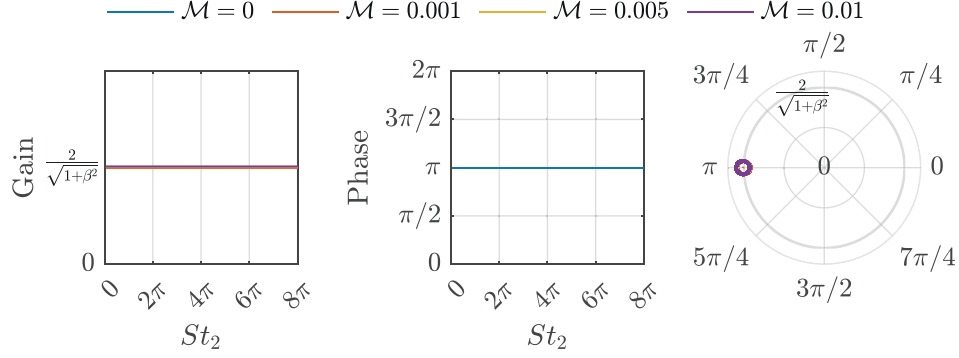$$\bar{F}_n = \frac{\hat{q}_n}{\lambda_n}. \tag{52}$$

Figure 6: Gain, phase and polar plot of the transfer function $\bar{F}_t = \hat{q}_t/\lambda_t$ plotted as a function of the modified Strouhal number $St_2 = St(1 + \beta^2)/\beta^2$, for different values of the non-dimensional Markstein length. The lines cannot be distinguished because they are all superimposed.
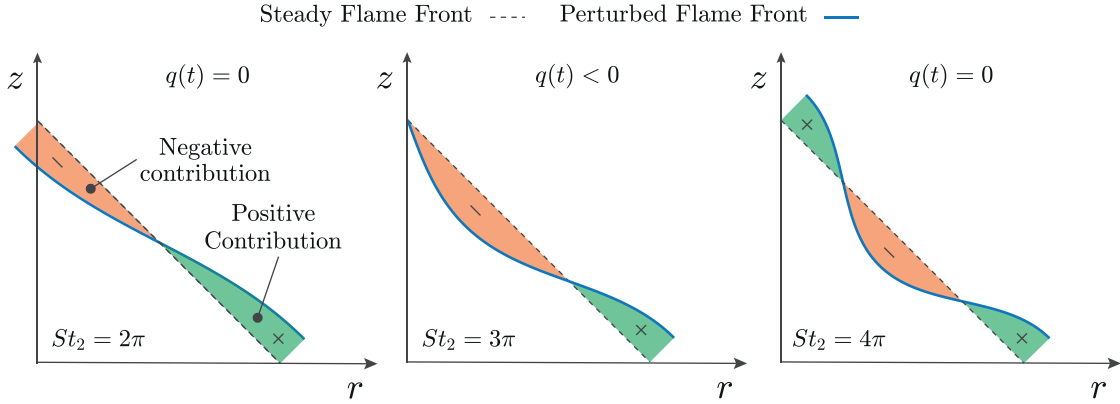

Figure 7: Diagram of the heat release rate perturbation, which in the linear approximation is proportional to the signed area that the perturbed flame front forms with the steady flame front. For simplicity, we report the case with non-dimensional Markstein length $\mathcal{M} = 0$. We observe that, for $St_2 = St(1+\beta^2)/\beta^2 = 2\pi$ and 4π the net area is zero and the heat release rate perturbation is also zero.

The flame-base coordinates $r_b(t)$ and $z_b(t)$ follow

$$r_b'(t) = \lambda_n \cos(\alpha)e^{i(St\,t+\phi_0)}, \qquad\qquad z_b'(t) = \lambda_n \sin(\alpha)e^{i(St\,t+\phi_0)}. \qquad (53a)$$

In this case, the flame-front is distorted by the flame-base motion. Perturbations starting from the flame base propagate towards the flame tip with constant phase speed. In the linear approximation, the heat release rate is proportional to the signed area that the perturbed flame front sweeps out with respect to the steady flame-front [?]. An extended explanation of this observation is reported in **??**. The diagram in figure **??** shows three snapshots of the perturbed flame-front corresponding to normal oscillations of the flame-base at Strouhal numbers $St_2 = 2\pi, 3\pi$ and 4π, respectively, with the non-dimensional Markstein length equal to zero. We observe that, when the Strouhal number St_2 is a multiple of 2π, the positive area portion balances the negative portion, resulting in zero heat release rate fluctuation. The diagram is also helpful for interpreting figure **??**, which shows the gain, phase and polar plot of the transfer function $\bar{F}_n$ for three values of the non-dimensional Markstein length $\mathcal{M}$.

We observe that when the Markstein length is zero (i.e. the flame speed does not depend on the flame stretch), perturbations created at the base of the flame propagate along the flame with constant amplitude. At $St_2 = 2n\pi$, where n is an integer, the fluctuation h.r.r. cancels out (figure **??**) so the gain is zero. For other St_2, the gain is non-zero. For zero Markstein length, the heat release rate can be expressed as a function of the flame-base displacement after a time delay τ, which is half the time that perturbations take to travel from the base to the tip.

When the Markstein length is non-zero (i.e. the flame speed depends on the flame curvature), flame surface perturbations reduce in amplitude as they convect towards the flame tip. Figure **??** shows three snapshots of the flame oscillations moving along the flame for the cases of non-dimensional Markstein length $\mathcal{M} = 0$ and $\mathcal{M} = 0.01$. We observe that, as the frequency of the oscillations increases, the flame tip becomes increasingly less perturbed, while the flame base remains perturbed. The spatial decay rate of the amplitude increases as the curvature increases, and therefore as the Strouhal number increases. This decay rate also increases as the Markstein length increases. This amplitude reduction means that the contribution to the fluctuating h.r.r. from the downstream part of the flame can no longer cancel the contribution from the base of the flame (see figure **??**). The contribution to the fluctuating h.r.r. therefore comes increasingly from the base of the flame, where the FTF has a fixed phase lag of $\pi/2$. This reveals that the flame has a constant time delay for zero Markstein length, but tends towards a constant phase delay for non-zero Markstein length as the Strouhal number increases.

We also analyse the influence of the flame aspect ratio, β, on the transfer function $\bar{F}_n$, when the Markstein length is non-zero. Figure **??** shows the gain, phase and polar plot of the transfer function $\bar{F}_n$ for three values of the flame aspect ratio: $\beta = 2$, 4 and 6. Due to the mechanism described in the preceding paragraph, as the Strouhal number increases, the contribution to fluctuating h.r.r. from the base of the flame becomes more influential than the contribution from the tip. The polar plot in figure **??** therefore resembles the polar plot in figure **??**, with the small difference that the origin is encircled once or more when the flame is longer (larger β). As the Strouhal number increases, the phase delay becomes $\pi/2$, as before. Note that this is plotted as $\pi/2 + n\pi$ for the longer flames, so that the lines of phase vs. Strouhal number are continuous, but that the addition of $n\pi$ is cosmetic. The same behaviour is seen in the measurements of the FTF in Fig. 7 in [**?**]. The important point is that, as the Strouhal number increases, the FTFs tend towards a constant phase delay of $\pi/2$, whatever the value of β.

4.3. Influence of the flame-base trajectory

In order to consider the contribution of the flame-base trajectory, we fit an ellipse (section **??**) to the experimental trajectory reported in figure 4 in [**?**], which was measured at $f = 100Hz$ and $\varepsilon = 0.1$. We determine the optimal values for the ellipse major axis length $\lambda = 0.6$, its aspect ratio $A_R = 0.04$, and angle $\theta = \pi/14$ by minimising the difference between the vertical and horizontal displacements from our model and the experimental data, as shown in figure **??**. Separately, the values of β, μ and $\mathcal{M}$ are estimated from the corresponding
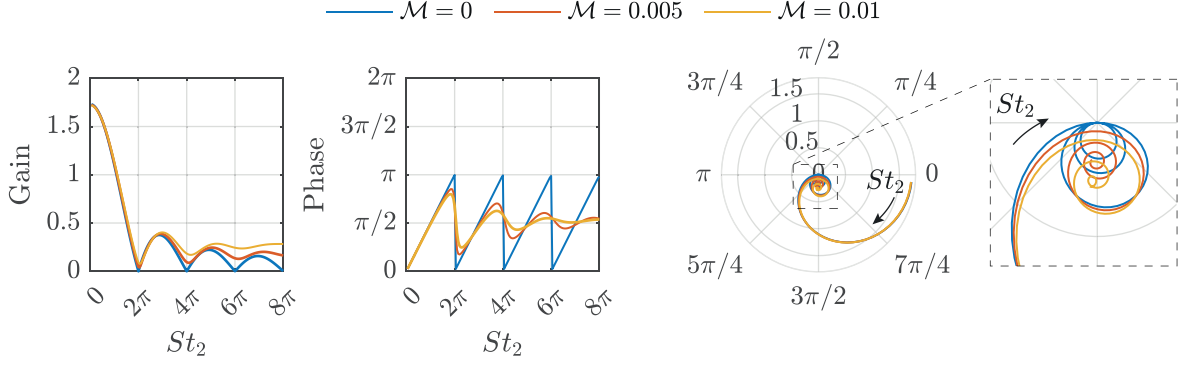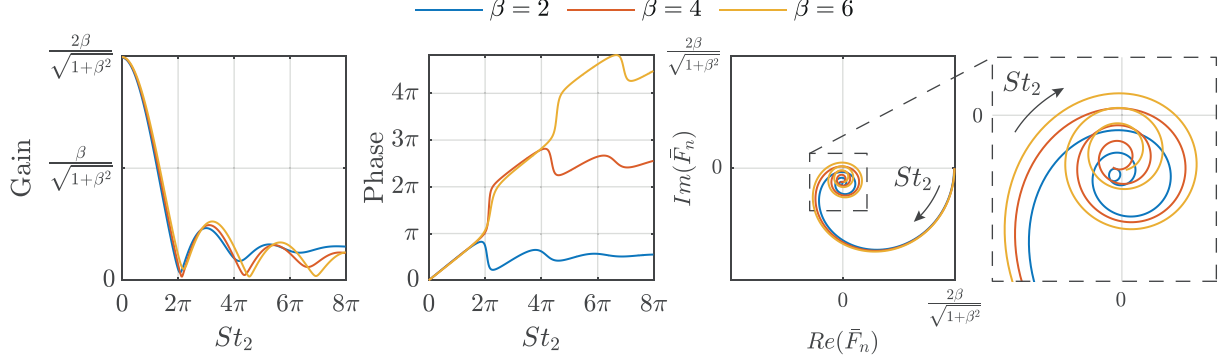
Figure 8: (Left to right) gain, phase and polar plot of the transfer function $\bar{F}_n = \hat{q}_n/\lambda_n$ plotted as a function of the modified Strouhal number $\mathrm{St}_2 = \mathrm{St}(1 + \beta^2)/\beta^2$, for different values of the non-dimensional Markstein length: $\mathcal{M} = 0$ (blue), 0.005 (red) and 0.01 (yellow). The value of the tip half-angle is equal to $\alpha = \pi/6$ ($\beta = \sqrt{3}$) to allow a direct comparison with figure 2 in [?]. In all cases the value of the gain goes to $2\beta/\sqrt{1 + \beta^2}$ when St approaches zero.
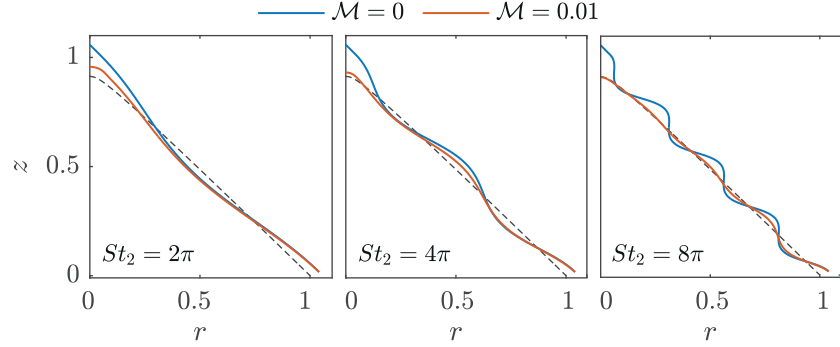
Figure 9: Snapshots of half of the flame-front perturbed by flame-base oscillations normal to the flame-front for three values of the modified Strouhal number $\mathrm{St}_2 = \mathrm{St}(1 + \beta^2)/\beta^2$: $\mathrm{St}_2 = 2\pi$, 4π and 8π and two values of the non-dimensional Markstein length $\mathcal{M} = 0$ and 0.01. The value of the flame aspect ratio β in this simulation is $\beta = 1$. The dashed lines show the steady flame front in the case with $\mathcal{M} = 0.01$. We observe that as the Strouhal number is increased, the upper part of the flame is not perturbed.

19

Figure 10: (Left to right) gain, phase and polar plot of the transfer function $\bar{F}_n = \hat{q}_n/\lambda_n$ plotted as a function of the modified Strouhal number $St_2 = St(1 + \beta^2)/\beta^2$, for different values of the aspect ratio: $\beta = 2$ (blue), 4 (red) and 6 (yellow). From left to right, we plot the gain and the phase; then we represent the transfer function by its real and imaginary part; finally, we show a magnification of the latter. The value of the non-dimensional Markstein length in this simulation is $\mathcal{M} = 0.01$.

steady flame, which is shown in figure 2.6 in [?]. The parameters $\beta = 3.873$, $\mu = 0.422$ and $\mathcal{M} = 0.0186$ fit the experimental image well (figure ?? left). We then set $K = K_f$ and calculate the FTF at $f = 100Hz$, corresponding to St ≈ 17, both ignoring and considering flame base oscillations.

In figure ?? (right) we plot the gain and phase of the flame transfer function FTF for three values of the aspect ratio A_R as a function of the inclination angle θ of the ellipse, where the major axis is fixed at $\lambda = 0.6$. The horizontal dashed lines correspond to the values of the gain and phase when the flame base contribution is ignored. The red circles refer to the parameters of the experimental trajectory in figure ??, and the triangles refer to the values of the gain and phase of the FTF when we simplify the flame-base trajectory to a straight line perpendicular to the flame front, ignoring the tangential component. We observe that neglecting the flame base contribution leads to a significant error in the prediction of the gain and phase of the flame transfer function. Furthermore, the angle, θ, of the trajectory has a large influence, while the aspect ratio A_R has a small influence. These results indicate that a simplified trajectory consisting of a straight line at the correct angle θ is sufficient when estimating the flame base contribution.

We can then simplify our calculation of the flame transfer function FTF with:

$$FTF = F_u + F_b, \tag{54}$$

where F_u is the contribution of the velocity field to the flame transfer function, with the flame base fixed and F_b is the contribution of the flame base oscillations, with the velocity field set to zero. Furthermore, the term F_b is given by the product $\bar{F}_b \cdot (\lambda/\hat{u})$, where $\bar{F}_b$ is the contribution to the FTF given by the shape of the trajectory followed by the flame base and is expressed as

$$\bar{F}_b = \frac{\hat{q}_t + \hat{q}_n}{\lambda} = \frac{\lambda_t}{\lambda}\bar{F}_t + \frac{\lambda_n}{\lambda}\bar{F}_n = \sin(\theta - \alpha)\bar{F}_t + \cos(\theta - \alpha)\bar{F}_n, \tag{55}$$
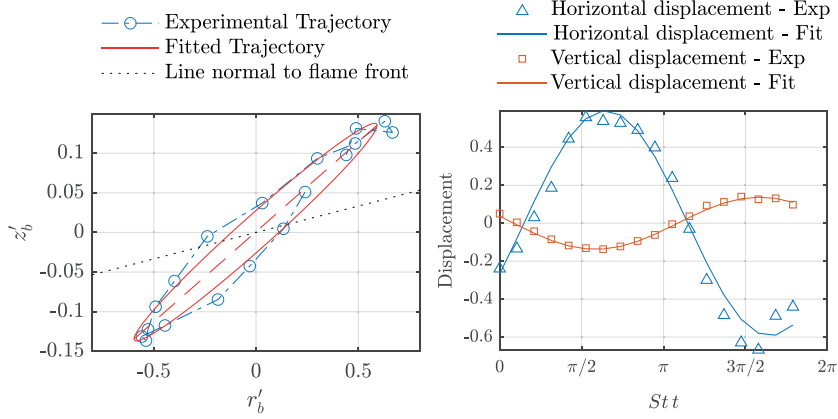
20

Figure 11: (Left) experimental flame-base trajectory shown in figure 4 in [?] fitted by an ellipse with parameters $\lambda = 0.6$, $\theta = \pi/14$ and $A_R = 0.04$; (right) comparison of the experimental and fitted flame-base displacement as a function of the phase angle of the oscillation.

and $(\lambda/\hat{u})$ is the transfer function linking acoustic fluctuations to the amplitude of the flame base oscillations. Figure **??** shows the gain and phase of the transfer function $\bar{F}_b$ versus the modified Strouhal number $St_2 = St(1 + \beta^2)/\beta^2$ for different values of the angle θ, with $\beta = 1$ and $\mathcal{M} = 0$. The transfer function $\bar{F}_b$ is the result of the linear combination of $\bar{F}_t$ and $\bar{F}_n$ as shown by equation (**??**). The transfer function is therefore heavily influenced by the angle of the flame base trajectory, as can be seen in figure **??**.

4.4. Modelling the flame transfer function as a time-delay

If the heat release rate fluctuations from a flame depend only on the fluctuating velocity, rather than fluctuating pressure or fluctuating composition, then the h.r.r. fluctuations must be slightly out of phase with the velocity fluctuations for the thermoacoustic mechanism to be active. The simplest physics-based model for this phase lag is a time delay between velocity perturbations at the base of a flame and subsequent h.r.r. fluctuations along the flame. This is known as the $n - \tau$ model and it dates back to the 1940's [?]. This time delay accounts for physical phenomena such as droplet break-up and evaporation, or (as in this paper) perturbations travelling down a flame sheet. In this case study, we note that the time delay between acoustic and heat release rate harmonic fluctuations must be interpreted as a relaxation time property rather than a net delay property because any perturbation on the flame front will immediately result in a heat-release rate perturbation. Modelling the flame response using a constant value of the time delay across harmonic forcing frequencies is attractively simple and is frequently used for premixed flames.

In section **??** we showed that, for flames with non-zero Markstein lengths, the h.r.r. fluctuations could not be modelled with such a time delay. This is because, if the flame speed increases with the flame curvature (i.e. at higher Strouhal numbers and higher Markstein lengths), perturbations decay as they travel downstream and only the base of the flame contributes to the fluctuating h.r.r. The time delay model, although simple, would not be
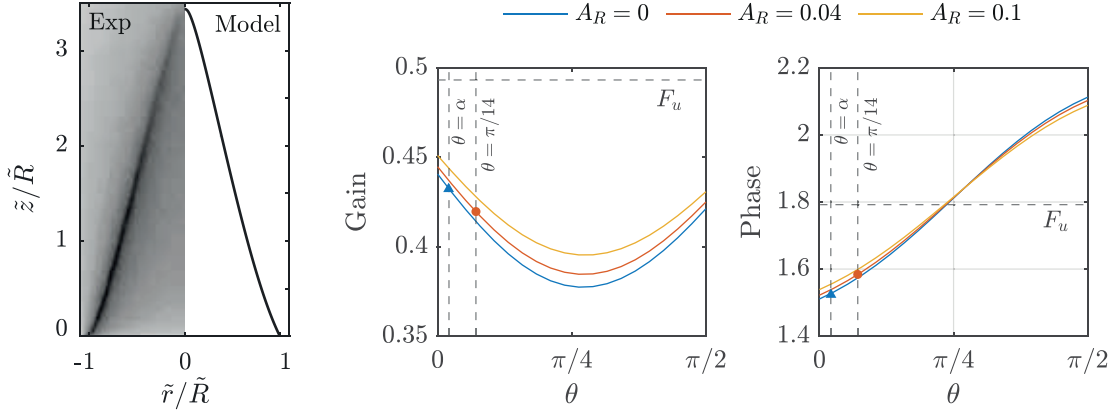
21

Figure 12: (Left) comparison of the experimental steady-state flame image in [**?**] corresponding to the same experimental setup used in the dynamical case where the flame base motion is tracked (figure **??**) and the steady-state flame obtained by the model developed in this work with $\beta = 3.87$, $\mu = 0.422$ and $\mathcal{M} = 0.0186$; (right) gain and phase of the FTF at St ≈ 17 ($f = 100 Hz$ in the experimental setup) versus the angle θ of the ellipse describing the flame base motion for different values of the aspect ratio A_R. The horizontal dashed lines correspond to the values of the gain and phase when the flame base is not moving. The circles correspond to the flame-base motion shown in figure **??** ($\theta = \alpha$, $A_R = 0$), and the triangles refer to the values of the gain and phase obtained when simplifying the flame-base trajectory to a straight line perpendicular to the flame steady-state at the base ($\theta = \alpha$, $A_R = 0$).
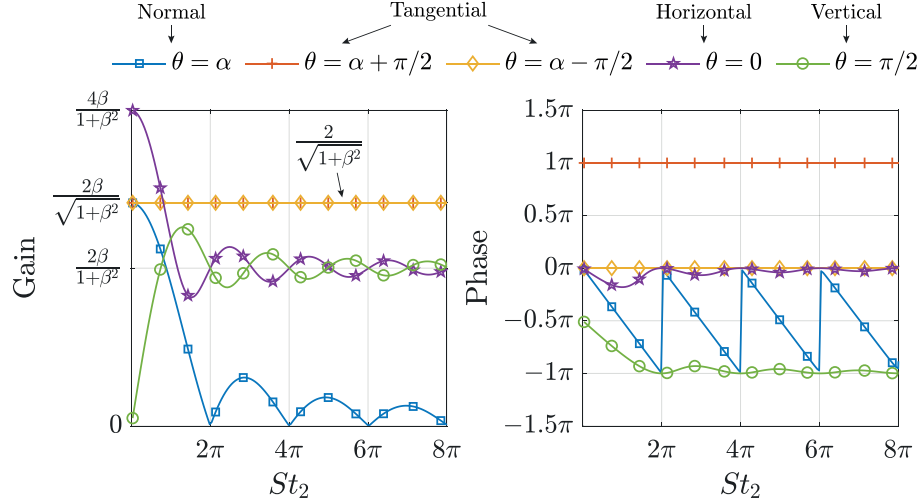
Figure 13: Gain and phase of the transfer function $\bar{F}_b = (\hat{q}_t + \hat{q}_n)/\lambda$ obtained by varying the angle θ of the flame-base trajectory, assumed as a straight line ($A_R = 0$). We consider normal and parallel motions as well as horizontal and vertical motions. The non-dimensional Markstein length is $\mathcal{M} = 0$ and the aspect ratio is $\beta = 1$.

a good model for this flame in general. It would only be justifiable if the Markstein length were zero.

In section ?? we explained that acoustic fluctuations at the burner rim result in both flame-base and velocity field perturbations. Every perturbation of the flame shape propagates from the base to the tip. When $\mathcal{M} = 0$ the convection speed of flame shape perturbations is $K_f = (1 + \beta^2)/\beta^2$. We define the characteristic time $T = 1/K_f$ as the time taken for a perturbation to travel from the flame-base to the flame-tip. When subjected to acoustic velocity fluctuations, the velocity field and the flame base are perturbed and both of these cause flame wrinkles that propagate from the base to the tip. The flame shape arises from the combined action of the velocity field and the convection of wrinkles. This can amplify, increase or even cancel the flame wrinkles [?]. The heat-release-rate perturbations are proportional to the signed area generated by the intersection of the perturbed and steady flame-fronts, as explained in section ?? and figure ??. The mechanism linking acoustic fluctuations to heat-release-perturbations in the Bunsen flame is illustrated in figure ??.
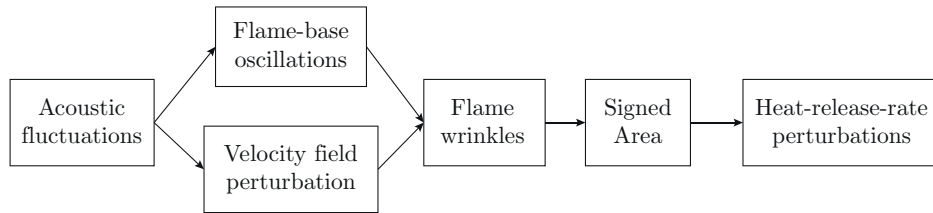
Figure 14: Diagram of the mechanism linking acoustic fluctuations to heat-release-rate perturbations in the Bunsen flame.

For illustration, we perform three simulations: (i) anchoring the flame-base and setting the value of the non-dimensional convective speed to $K = K_f$, F_u; (ii) setting the velocity field perturbation to zero and forcing the flame-base to oscillate in the normal direction, $\bar{F}_n$ and (iii) simulation (i) but allowing the non-dimensional convective speed to vary. We set the non-dimensional Markstein length $\mathcal{M} = 0$ and use $\beta = 1$.

Simulations (i) and (ii) are compared in figure ??. When the value of the non-dimensional convective speed is set to $K = K_f$ the velocity field and flame wrinkle convection are in phase. Therefore, when the flame is subjected to harmonic acoustic forcing, the flame wrinkles are amplified as they are convected towards the tip, as shown in figure ?? (bottom). If we compare the phase of the Transfer Functions in figure ?? (top), we see that the time delay associated with case (i) is equal to T because the flame tip contributes most to heat release rate fluctuations, whereas the time delay associated with case (ii) is $T/2$ because each part of the flame surface contributes equally to heat release rate fluctuations. The third kind of simulation is performed by setting $K = K_f, 1/2K_f, 5K_f$. In figure ??, we show the Transfer Functions alongside the flame wrinkles for three values of the modified Strouhal number $\text{St}_2 = \pi, 3\pi, 5\pi$. The interaction between the convection of the flame wrinkles with the

velocity field varies with K/K_f. When $K = K_f$, $\tau = T$ but when $K = 5K_f$, the envelope of the flame wrinkles is uniform along the flame-front and the time delay tends to $T/2$ as for the flame-base oscillations case described above.
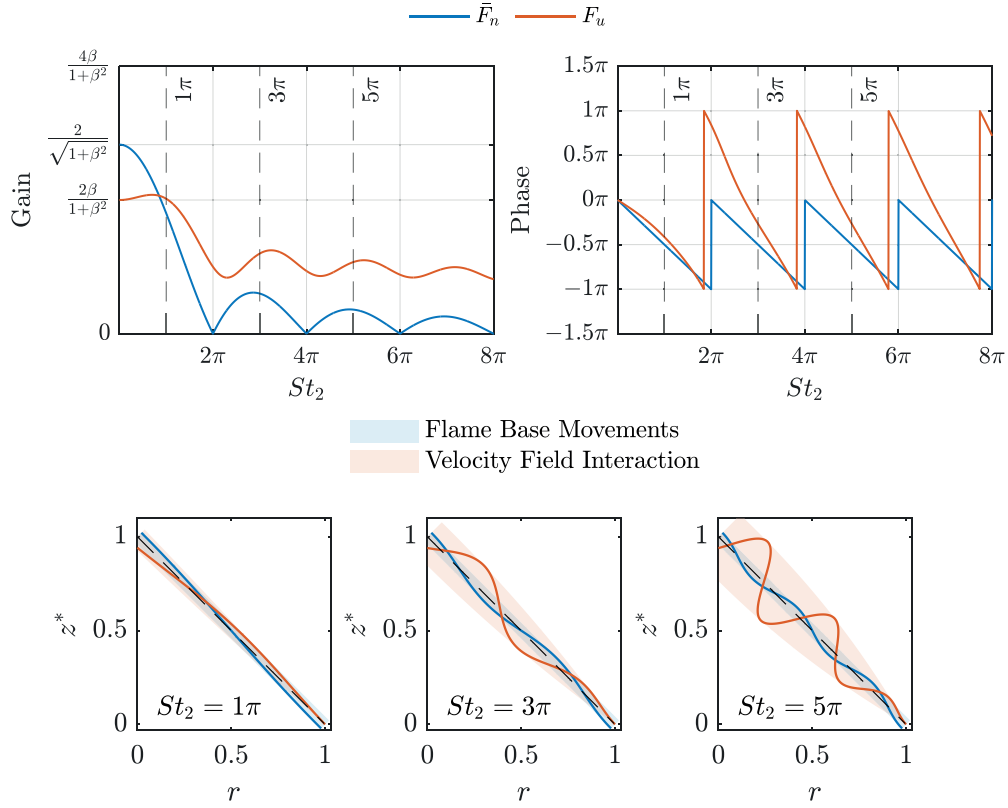

Figure 15: (Top) Gain and phase of the Transfer Functions F_u and $\bar{F}_n$. (Bottom) Envelopes of the perturbed flame in the two cases with a forcing Strouhal number $St_2 = \pi$, 3π and 5π, with $\varepsilon = 0.03$. With this set of parameters, the envelope of the velocity field case are more pronounced at the tip of the flame. The envelope of the flame-base case shows that perturbations created at the base of the flame propagate along the flame without any reduction in amplitude. The slope of the phase plot on the right show that the time delay for the velocity field case is twice the time delay of the flame-base case.

In summary, even when the Markstein length is zero, the time delay τ can vary in the range $\tau = [0, T]$, depending on the Strouhal number and on whether the flame motion depends mainly on the velocity field, the flame base movement, or a combination of the two. Even for this simple Bunsen flame, a model with a single time delay is not valid. Instead, the flame dynamics must either be simulated or modelled with a more elaborate model. These results are in line with the observations of Blumenthal et al. [?], which state that conical premixed flames are better represented by a distribution of time lags rather than a single time delay.
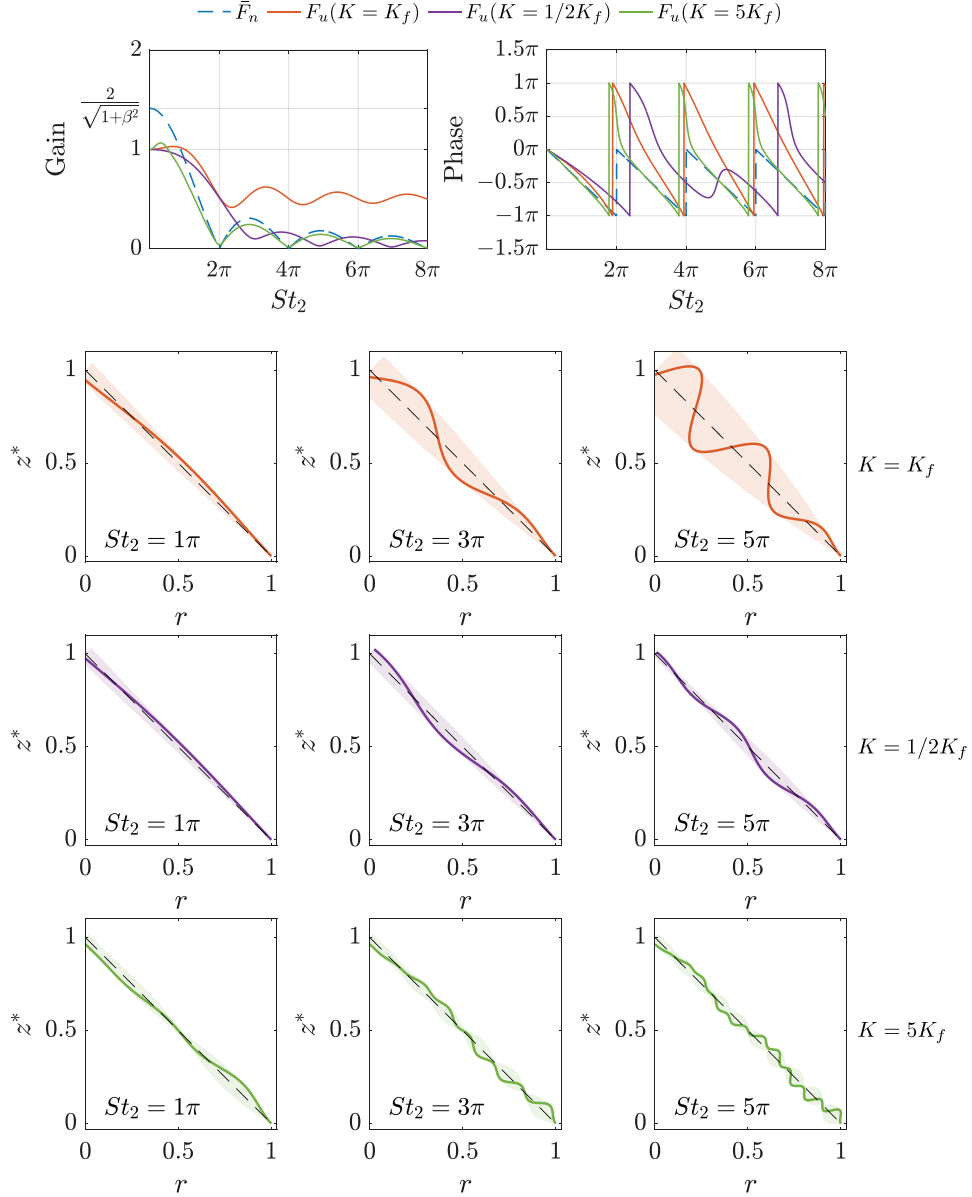
Figure 16: (Top) Gain and phase of the Transfer Functions $\bar{F}_n$ and F_u with $K = K_f, 1/2K_f, 5K_f$. (Bottom) Flame envelope for 3 values of the Strouhal number St_2, using $\varepsilon = 0.03$. Comparing the envelopes with the phase it is clear that when the perturbation is uniformly distributed along the flame front, the transfer functions become similar to the one related to the flame-base motions (dashed line).

.

5. Conclusions

In this study, we create a general model for the tracking of a premixed flame sheet. This model is based on a Lagrangian formulation of the interface motion and is more computationally efficient than the level-set formulation solved on a grid. This model has been applied to a conical Bunsen flame and has been validated against Orchini and Juniper [?] who included the curvature effect on the flame dynamics but assumed that the flame-base is attached to the burner rim, and against Cuquel et al. [?], who neglected the flame-stretch influence and assumed that the flame-base oscillates normal to the flame front direction only. These are special cases of the general model presented here.

We have demonstrated that the flame front dynamics, the heat release rate perturbations, and the flame transfer function FTF contain three contributions: (i) the velocity field locally perturbing the flame-front, (ii) the flame-base oscillations normal to the steady flame-front, which propagate along the flame from the base to the tip and (iii) the flame-base oscillations tangential to the flame-front, reducing and amplifying the flame-length.

When we include the effect of the flame-stretch, increasing the frequency of the oscillations, the flame wrinkles decay with downstream distance, as observed by Preetham et al. [?]. When the frequency is large enough, the tip of the flame barely oscillates and, as we increase the frequency, the region of the flame affected by wrinkles reduces and the phase shift saturates towards a constant value, as found experimentally in [?]. In this case, the time delay associated with the FTF reduces with the frequency and this has a clear physical cause: the perturbations take less time to reach the point at which they disappear and this point no longer coincides with the flame tip. Experimental studies [? ?] have shown that the flame-base follows an approximately elliptical trajectory. For the trajectory taken from [?], we show that the aspect ratio of this elliptical trajectory has little influence on the FTF, but that the angle has a significant influence. We conclude that the flame-base trajectory can be well approximated by a straight line, but the angle with respect to the flame-front must be specified. Finally, we show why a simple $n - \tau$ model, with fixed τ, will not work even for this simple flame. This demonstrates that, when building a quantitatively-accurate model of a thermocaoustic system containing this flame, the flame dynamics will need either to be simulated or to be modelled with a more elaborate model than a simple $n - \tau$ model.

The flame model used in this paper can capture the numerically and experimentally-observed behaviour in [?] and [?], and has been designed to be differentiable, meaning that the gradient of the model output can be calculated with respect to the model parameters. Differentiable codes can be used for rapid data assimilation using Laplace's method [?], meaning that this code can be used to assimilate model parameters from experimental observations of a Bunsen flame. This code is provided with the paper, allowing the user to generate the FTF of a conical premixed flame with any flame aspect ratio β, any Markstein length $\mathcal{M}$, any convective speed ratio K and any flame-base trajectory.

6. Acknowledgements

Appendix A. Governing equations in non-dimensional form

The non-dimensional governing nonlinear system of equations (**??**) is expressed by

$$
\partial_t r = \frac{\beta^2(\partial_\eta z)}{\sqrt{(\partial_\eta r)^2 + \beta^2(\partial_\eta z)^2}} \left(\frac{\beta(\partial_\eta z)}{\sqrt{(\partial_\eta r)^2 + \beta^2(\partial_\eta z)^2}} v_r - \frac{(\partial_\eta r)}{\sqrt{(\partial_\eta r)^2 + \beta^2(\partial_\eta z)^2}} v_z \right.
$$
$$
\left. + \frac{1}{\sqrt{1+\beta^2}} \left(1 - \mathcal{M}\beta^2 \left(\frac{(\partial_\eta r)(\partial_{\eta\eta} z) - (\partial_{\eta\eta} r)(\partial_\eta z)}{\left((\partial_\eta r)^2 + \beta^2(\partial_\eta z)^2\right)^{3/2}} + \frac{1}{r}\frac{(\partial_\eta z)}{\sqrt{(\partial_\eta r)^2 + \beta^2(\partial_\eta z)^2}} \right) \right) \right),
$$
$$
\partial_t z = -\frac{(\partial_\eta r)}{\sqrt{(\partial_\eta r)^2 + \beta^2(\partial_\eta z)^2}} \left(\frac{\beta(\partial_\eta z)}{\sqrt{(\partial_\eta r)^2 + \beta^2(\partial_\eta z)^2}} v_r - \frac{(\partial_\eta r)}{\sqrt{(\partial_\eta r)^2 + \beta^2(\partial_\eta z)^2}} v_z \right.
$$
$$
\left. + \frac{1}{\sqrt{1+\beta^2}} \left(1 - \mathcal{M}\beta^2 \left(\frac{(\partial_\eta r)(\partial_{\eta\eta} z) - (\partial_{\eta\eta} r)(\partial_\eta z)}{\left((\partial_\eta r)^2 + \beta^2(\partial_\eta z)^2\right)^{3/2}} + \frac{1}{r}\frac{(\partial_\eta z)}{\sqrt{(\partial_\eta r)^2 + \beta^2(\partial_\eta z)^2}} \right) \right) \right),
$$

where

$$
v_r = -\varepsilon r \frac{K \mathrm{St}}{2\beta} \sin\left(\mathrm{St}(t - Kz)\right),
$$
$$
v_z = \left(1 + \mu(1 - 2r^2)\right) + \varepsilon \cos\left(\mathrm{St}(t - Kz)\right),
$$

are the radial and longitudinal component of the velocity field, respectively.

Appendix B. Validations
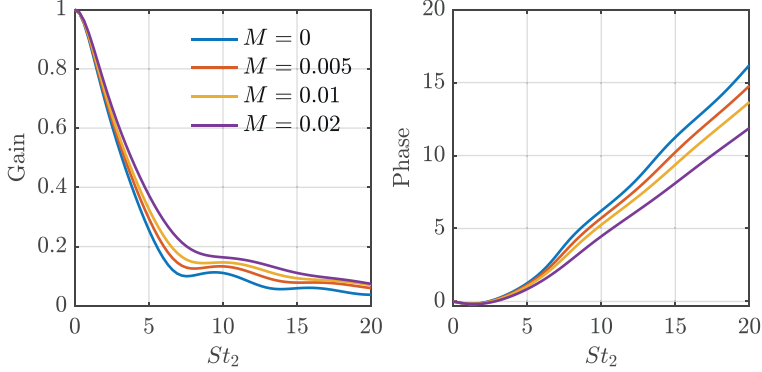
We validate the linear code in four steps.

Figure B.17: Flame transfer functions FTFs during step 1 of the validation. The flame base is attached to the burner rim and we vary the Markstein length $\mathcal{M}$ while setting $\beta = 6$ and $\eta = 1.1$. The results match those in figure 5 in [?].

1. In the first step, we compute the flame transfer functions for $\mathcal{M} = 0$, 0.005, 0.01, 0.02. We anchor the flame-base to the burner rim and set the other parameters to $\beta = 6$, $\eta = 1.1$ and $\mu = 0$. The results are shown in figure ?? and match those reported in figure 5 in [?].
2. In the second step, we compute the Flame-Base Transfer Function $\bar{F}_b$ for $\beta = 1$, 3, 6. We force the flame-base to oscillate in the longitudinal direction ($\theta = \pi/2$). We set the Markstein length $\mathcal{M} = 0$ and compare the results with the analytical solution:

$$\bar{F}_b = \frac{2\beta}{1 + \beta^2} \left(\frac{1}{i\,\mathrm{St}_2} \left(1 - \mathrm{e}^{-i\,\mathrm{St}_2}\right) - 1 \right). \tag{B.1}$$

   The results are shown in figure ??.
3. In the third step, we compute the Flame-Base Transfer Function $\bar{F}_b$ for $\alpha = \mathrm{atan}(1/\beta) = \pi/12$, $\pi/6$, $\pi/3$. We force the flame-base to oscillate in the direction perpendicular to the flame front ($\theta = \alpha$). We set the Markstein length $\mathcal{M} = 0$. In this case we can compare the results shown in figure ?? with figure 2a in [?].
4. In the fourth step, we compare the linear results of the flame transfer function FTF with the nonlinear results of the flame describing function FDF. We set the amplitude of the velocity field perturbation to $\varepsilon = 10^{-3}$, 10^{-2}, 10^{-1}. We set the Markstein length $\mathcal{M} = 0.02$, $\beta = 6$ and $\eta = 1.1$. In figure ?? we show that as the amplitude of the forcing goes to zero, the FDFs converge to the FTF.

Appendix C. Signed-area interpretation of the heat release rate fluctuations

The total heat release rate of the flame $\tilde{q}(\tilde{t})$, in dimensional form, is expressed as:

$$\tilde{q}(\tilde{t}) = \int_{\partial\Omega} \tilde{\rho}_R \tilde{S}_f \tilde{h}_R \mathrm{d}\tilde{A}, \tag{??}$$
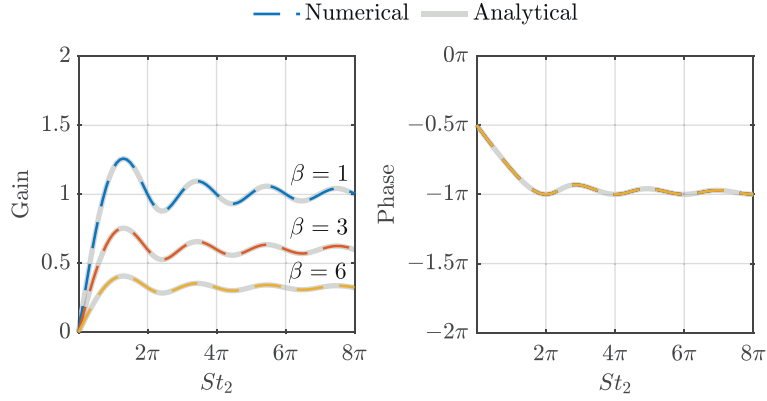
Figure B.18: Flame-Base Transfer Functions $\bar{F}_b$ during step 2 of the validation. The velocity field is set to zero and we force the flame base to oscillate in the longitudinal direction ($\theta = \pi/2$). We vary the value of β and set the Markstein length $\mathcal{M} = 0$ so that we can compare the results with the analytical solution of equation (**??**).
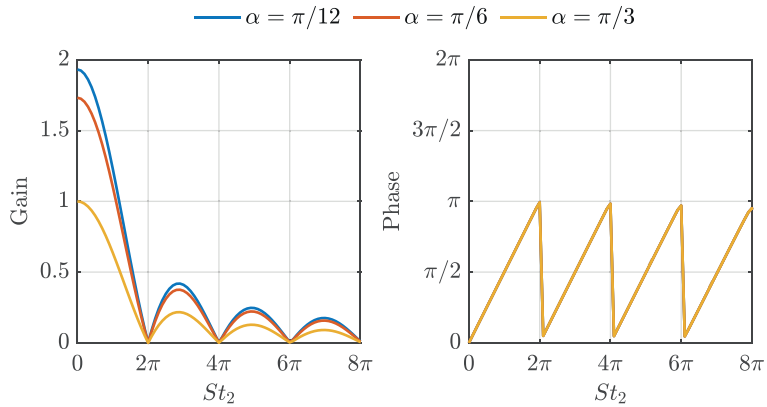

Figure B.19: The flame-Base Transfer Function $\bar{F}_b$ during step 3 of validation. The velocity field is set to zero and we force the flame base to oscillate in the normal direction with respect to the flame front ($\theta = \alpha$). We vary the value of α and set the Markstein length $\mathcal{M} = 0$. The results match those reported in figure 2a of [**?**].
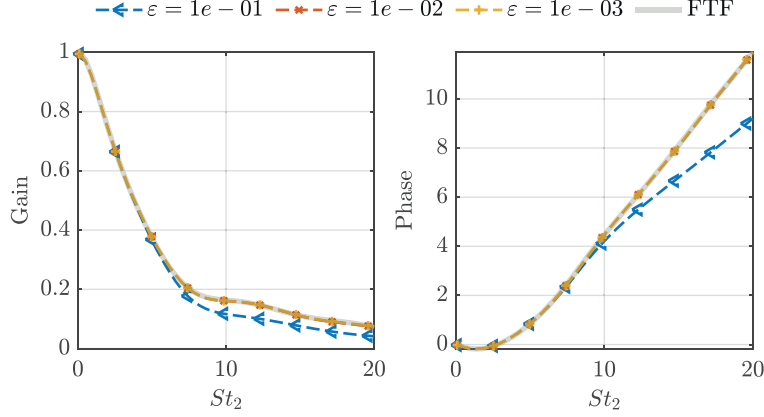
Figure B.20: Comparison of the Flame Describing Function FDF with the flame transfer function FTF during step 4 of validation. The flame base is attached to the burner rim and we vary the amplitude of the velocity field perturbation ε while setting $\beta = 6$, $\mathcal{M} = 0.02$ and $\eta = 1.1$. The FDF converges to the FTF as ε goes to zero.

where $\partial\Omega$ is the total flame area, $\tilde{\rho}_R$ is the reactant's density, $\tilde{h}_R$ is the heat release rate per unit mass of burnt reactants, and $\mathrm{d}\tilde{A}$ is an infinitesimal flame area expressed as $\mathrm{d}\tilde{A} = \tilde{r}\mathrm{d}\theta\mathrm{d}\tilde{l}$. If we consider the case with Markstein length equal to $\tilde{\mathcal{M}} = 0$, the heat release rate $\tilde{q}(t)$ is proportional to

$$\tilde{q}(t) \propto \int_{\partial\Omega} \mathrm{d}\tilde{A} = 2\pi \int_L \tilde{r}\mathrm{d}\tilde{l}. \tag{C.1}$$

We define a local reference frame $X - Y$ whose origin is the flame apex and the X-axis is aligned to the flame front in steady condition, as shown in figure **??**. The radial coordinate of the perturbed flame front is

$$\tilde{r} = X \sin(\alpha) + Y(X) \cos(\alpha), \tag{C.2}$$

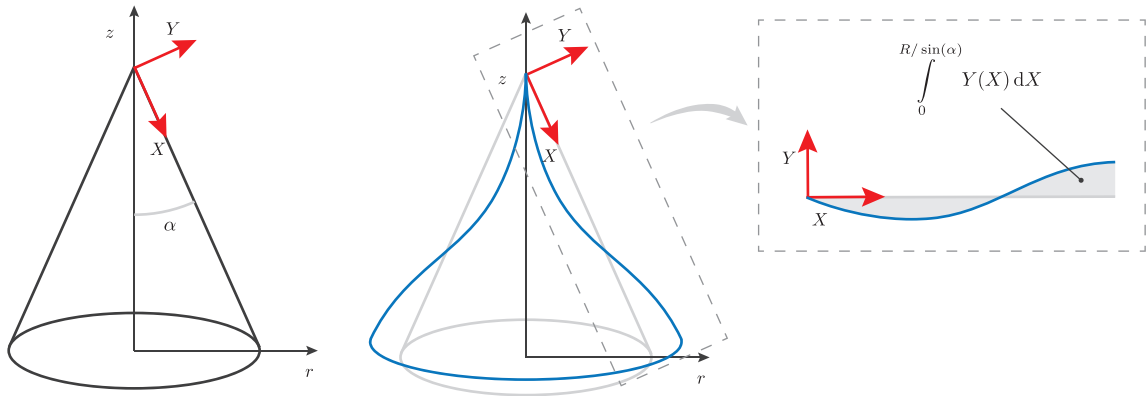where α is the cone angle and $Y(X)$ is the perturbed flame front coordinate. In the linear approximation,

$$\mathrm{d}\tilde{l} \approx \mathrm{d}X$$

Hence substituting these expressions in (**??**) we obtain

$$\tilde{q}(\tilde{t}) \propto 2\pi \int_0^{\tilde{R}/sin(\alpha)} (X \sin(\alpha) + Y(X) \cos(\alpha)) \, \mathrm{d}X$$

$$\propto \underbrace{\frac{\pi\tilde{R}^2}{\sin(\alpha)}}_{\text{steady}} + \underbrace{2\pi \cos(\alpha) \int_0^{\tilde{R}/sin(\alpha)} Y(X)\mathrm{d}X}_{\text{unsteady}}. \tag{C.3}$$

Therefore the unsteady part of the heat release rate q' is proportional to the signed area of

$$\tilde{q}'(\tilde{t}) \propto \int_0^{\tilde{R}/\sin(\alpha)} Y(X)\mathrm{d}X$$

30

(a) Steady flame-front

(b) Perturbed flame-front

Figure C.21: Digram of the signed area interpretation of the heat release rate perturbation.

.